

Adaptive Domain Decomposition Physics-Informed Neural Networks for Traffic State Estimation with Sparse Sensor Data

Eunhan Ka^a, Ludovic Leclercq^b, Satish V. Ukkusuri^{a,*}

^a*Lyles School of Civil and Construction Engineering, Purdue University, 610 Purdue Mall, West Lafayette, 47907, IN, United States*

^b*Univ Gustave Eiffel, ENTPE, LICIT-ECO7, Lyon, F-69675, France*

Abstract

Traffic state estimation from sparse fixed sensors is challenging because physics-informed neural networks (PINNs) tend to over-smooth the shock-waves admitted by the Lighthill-Whitham-Richards (LWR) model. This study proposes Adaptive Domain Decomposition Physics-Informed Neural Networks (ADD-PINN), a two-stage residual-guided framework for LWR-based offline speed-field reconstruction. A coarse global PINN is first trained; its spatial residual profile is then used to place subdomain boundaries and initialize child subnetworks in a decomposition-enabled mode, while a data-driven shock indicator can retain a single-domain fallback when localized evidence of transition is weak. The primary offline I-24 MOTION evaluation spans five days, five sensor configurations, and ten seeds per configuration, yielding 1,500 runs in total. Against neural and physics-informed baselines, ADD-PINN attains the lowest relative L_2 error in 18 of 25 configurations and in 14 of 15 sparse-sensing cases, while training 2.4 times faster than the extended PINN (XPINN) baseline. An ablation study supports spatial-only decomposition as an effective default for fixed-sensor traffic reconstruction in the evaluated settings. Supplementary Next Generation Simulation (NGSIM) experiments serve as a negative control: the shock indicator suppresses decomposition in all 50 runs, and the default single-domain fallback ranks first across all sensor configurations.

*Corresponding author

Email address: sukkusur@purdue.edu (Satish V. Ukkusuri)

These results support residual-guided spatial decomposition as an effective PINN-family design for offline reconstruction when sparse fixed sensing coincides with localized transition regions.

Keywords: Traffic State Estimation, Physics-Informed Neural Networks, Domain Decomposition, Two-Stage Learning, Sparse Sensor Data

1. Introduction

Traffic state estimation (TSE) is the process of inferring complete spatiotemporal fields of traffic variables (density, flow, and speed) from partial observations collected by fixed sensors such as loop detectors and cameras (Seo and Kusakabe, 2015; Seo et al., 2017). Accurate TSE underpins real-time traffic management, traveler information systems, and transportation infrastructure planning. In practice, sensor deployment is constrained by cost and maintenance: a typical freeway corridor may be instrumented with only a small number of detector stations spaced several miles apart, yielding sparse spatial coverage of the roadway. Reconstructing the full traffic state from such limited observations remains a fundamental challenge, particularly during incidents and rapidly evolving congestion.

Physics-based models provide a principled foundation for TSE. The Lighthill-Whitham-Richards (LWR) model (Lighthill and Whitham, 1955; Richards, 1956), a first-order hyperbolic conservation law, describes the spatiotemporal evolution of traffic density through mass conservation and a flow-density fundamental relation. Once closed by a fundamental relation, the LWR model predicts kinematic wave propagation, including the formation and dissipation of shockwaves at congestion boundaries. Model-based data assimilation methods, such as extended Kalman filtering (Wang and Papageorgiou, 2005; Wang et al., 2008), combine these macroscopic traffic models with real-time sensor data to reconstruct traffic states. Variational and Hamilton-Jacobi formulations provide a complementary line of exact or optimization-based estimation for heterogeneous sensing settings (Daganzo, 2006; Canepa and Claudel, 2017). However, LWR and its higher-order extensions such as the Aw-Rascle-Zhang (ARZ) model (Aw and Rascle, 2000; Zhang, 2002) rely on idealized assumptions that limit fidelity under real-world conditions. Data-driven approaches, including deep learning models for traffic speed prediction and imputation (Ma et al., 2015; Wu et al., 2018), can learn complex spatiotemporal patterns but require large

volumes of high-quality training data and provide no guarantee of physical consistency.

Physics-informed neural networks (PINNs) address this trade-off by embedding the governing partial differential equations (PDEs) directly into the neural network’s training objective (Raissi et al., 2019). The resulting model simultaneously fits available sensor data and satisfies the traffic flow PDE at collocation points throughout the domain, enabling physically consistent estimation even in regions with no direct observations. Several studies have demonstrated the promise of PINNs and related physics-informed learning methods for freeway TSE with the LWR and ARZ models (Shi et al., 2022, 2021; Yuan et al., 2021a; Huang and Agarwal, 2022). Despite these advances, standard PINNs face several challenges when applied to traffic flow. First, neural networks exhibit *spectral bias*, a tendency to learn smooth, low-frequency functions, limiting their ability to represent the sharp discontinuities characteristic of LWR solutions (Tancik et al., 2020). Second, balancing the data loss and PDE loss during training is difficult; inappropriate weighting biases the model toward either underfitting the physics or underfitting the data (Wang et al., 2021). Beyond these optimization challenges, the strong-form PDE residual is ill-defined at discontinuities. Pointwise residual minimization is therefore structurally incompatible with the shock solutions admitted by hyperbolic conservation laws such as LWR. These structural difficulties are visible in real freeway data. Figure 1 shows a representative ground-truth speed field from the I-24 MOTION dataset, with sharp spatial gradients across shock fronts and high-frequency temporal variation throughout the congested window. This localized multi-scale structure can be difficult for a single global PINN to resolve under sparse fixed-sensor supervision. Lei et al. (2025) recently formalized these failure modes, showing that PINNs can perform worse than both their data-driven and physics-based counterparts when spatiotemporal resolution is insufficient or gradient imbalance is severe.

Domain decomposition mitigates spectral bias: partitioning the spatiotemporal domain into smaller subdomains, each handled by a dedicated sub-network, reduces the local function complexity that any single network must represent. The extended PINNs (XPINNs) framework (Jagtap and Karniadakis, 2020) generalizes this idea to arbitrary PDEs by decomposing the domain in both space and time and enforcing residual-based continuity at subdomain interfaces. We adopt XPINN as our DD-PINN baseline because it supports spatial, temporal, and space-time decomposition within

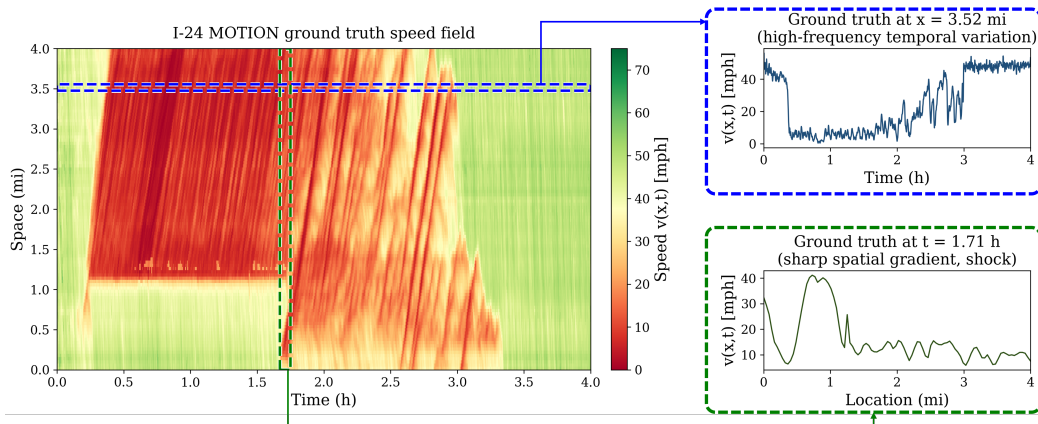


Figure 1: Ground-truth speed field $u(x, t)$ from I-24 MOTION on 2022-11-21 (left), with a temporal trace at $x = 3.52$ mi (top right) and a spatial profile at $t = 1.71$ h (bottom right). Congested regions appear in red and free-flow regions in green.

a unified framework, enabling systematic comparison of decomposition directions. Residual-based adaptive refinement (RAR) complements domain decomposition by concentrating collocation points in high-error regions (Wu et al., 2023). However, canonical DD-PINN frameworks and many subsequent variants still depend on user-designed or initialization-dependent decompositions (Jagtap and Karniadakis, 2020; Moseley et al., 2023; Hu et al., 2023). More recent adaptive approaches have begun to relax this assumption (Peng et al., 2025; Si and Yan, 2025; Luo et al., 2025; Botvinick-Greenhouse et al., 2025); however, these methods target generic PDE benchmarks rather than sparse fixed-sensor traffic state estimation, and they do not study the decomposition direction under fixed-sensor observability. The choice of decomposition direction (spatial, temporal, or space-time) has received limited attention for fixed-sensor traffic state estimation, even though the answer depends strongly on the observation structure and the underlying PDE.

Huang and Agarwal (2023) demonstrated the shockwave challenge explicitly for traffic, showing that physics-informed learning on the hyperbolic LWR equation produces errors substantially larger than on a diffusion-augmented counterpart when solutions contain shockwaves. This result motivates methods that resolve discontinuities without sacrificing the hyperbolic character of the conservation law. It also motivates approaches that localize shock-prone

transition regions rather than relying on a single global network, artificial smoothing, or direct tracking of a moving shock manifold.

Motivated by these limitations, we develop ADD-PINN, a two-stage residual-guided framework that trains a coarse global PINN, uses an observed-data shock indicator to avoid unnecessary decomposition when localized transition evidence is weak, uses the spatial residual profile to place split positions when decomposition is enabled, initializes child networks from the parent weights, and applies conservation-aware coupling across fixed artificial interfaces. The framework localizes regions where a single global PINN struggles to represent the LWR dynamics. We make four contributions:

1. **Two-stage residual-guided DD-PINN for sparse fixed-sensor reconstruction.** ADD-PINN first trains a coarse global PINN, uses an observed-data shock indicator to avoid unnecessary decomposition when localized transition evidence is weak, and uses the coarse spatial residual profile to place split positions when decomposition is enabled. Parent-to-child warm start and conservation-aware fixed-interface coupling are integrated into the same traffic-specific workflow.
2. **Decomposition-direction analysis under fixed-sensor observability.** A controlled comparison of spatial, temporal, and space-time decomposition, supported by three rationales (shockwave geometry, data-coverage asymmetry, residual anisotropy) and a 120-run ablation, supports spatial-only decomposition as an effective default in the evaluated fixed-sensor freeway settings.
3. **Accuracy-efficiency improvement through coarse-to-fine training.** Parent-to-child weight transfer enables warm-start fine-tuning of fewer subdomains, yielding lower mean error and 2.4 times faster training than a standard XPINN baseline in the evaluated I-24 configurations.
4. **Multi-day real-world validation within PINN-family estimators.** A 1,500-run evaluation on five I-24 MOTION days, five sensor configurations, and ten seeds, together with a supplementary NGSIM negative-control experiment, provides a large-sample assessment of residual-guided DD-PINN design for traffic state reconstruction.

The experimental benchmark is intentionally bounded to neural and physics-informed estimators. Matched comparison with classical TSE

estimators, including extended Kalman filtering, adaptive smoothing, and variational Hamilton-Jacobi reconstruction, requires distinct calibration and observation-model assumptions and is treated as a complementary direction in Section 6.3.

The remainder of this paper is organized as follows. Section 2 reviews relevant literature on TSE methods, PINNs, domain decomposition PINNs, and PINNs for conservation laws. Section 3 presents the ADD-PINN methodology, including the two-stage training framework, adaptive subdomain detection, interface conditions, and decomposition direction analysis. Section 4 describes the datasets, baselines, and evaluation protocol. Section 5 reports quantitative results. Section 6 discusses findings and implications. Section 7 concludes.

2. Literature Review

2.1. Traffic State Estimation Methods

Traffic state estimation methods are commonly categorized as model-based, data-driven, physics-informed, or hybrid.

Model-based approaches. Classical model-based TSE relies on macroscopic traffic flow models combined with filtering, smoothing, or variational inference. The LWR conservation law (Lighthill and Whitham, 1955; Richards, 1956), closed by an empirical fundamental relation, remains a common backbone of physics at the corridor scale. The Cell Transmission Model (Daganzo, 1994) provided a computationally practical, discrete analog of the LWR that reproduces queues and shockwave propagation, and became a core tool for freeway TSE, filtering, and control. Real-time estimation has relied heavily on extended Kalman filtering and related assimilation methods that combine macroscopic process models with sensor observations (Wang and Papageorgiou, 2005; Wang et al., 2008). Treiber and Helbing (2002) introduced an adaptive smoothing method for detector-based spatiotemporal traffic reconstruction, which has become a benchmark in the field. Variational and Hamilton-Jacobi formulations provide a complementary line of work by exploiting cumulative-count representations and semi-analytic solution structures to enable exact or optimization-based data assimilation with heterogeneous observations (Daganzo, 2006; Canepa and Claudel, 2017). Seo et al. (2017) provide a comprehensive survey classifying TSE approaches by data source, state variable, and estimation paradigm. While model-based

methods are physically grounded, they depend on calibration quality and typically assume a fixed or low-dimensional traffic law that may be insufficient to capture the complexity of real traffic dynamics.

Data-driven approaches. Much of the traffic machine learning literature has focused on prediction or imputation rather than direct reconstruction of complete traffic fields. Recurrent neural networks, such as long short-term memory models and hybrid deep architectures, can learn spatiotemporal dependencies from historical sensor data (Ma et al., 2015; Wu et al., 2018). More directly related to TSE, Rempe et al. (2022) used deep convolutional neural networks to estimate continuous speed fields from sparse freeway data. These methods can capture nonlinear traffic patterns directly from observations, but they require representative training data and provide no guarantee of conservation, physically admissible wave propagation, or robustness in unobserved regions.

Physics-informed and hybrid approaches. Physics-informed neural networks (PINNs) and related physics-informed deep learning (PIDL) methods aim to combine the data efficiency of physical models with the representational power of neural networks. Huang and Agarwal (2022) demonstrated that embedding the LWR PDE into the training objective significantly improves estimation accuracy under sparse sensing. Shi et al. (2022) and Shi et al. (2021) applied physics-informed learning to both first-order and second-order traffic models, showing that shockwave formation and dissipation patterns can be reconstructed from limited data. Barreau et al. (2021) used physics-informed learning with pretraining to reconstruct traffic density from low-penetration probe vehicles. Beyond standard PINNs, Lu et al. (2023) and Zhang et al. (2024) coupled traffic-flow models with differentiable computational graphs to jointly estimate corridor states, queue profiles, and fundamental-diagram parameters, while Zhao and Yu (2024) combined a PDE observer with deep learning for boundary-sensing TSE. Ka et al. (2024) further extended physics-informed estimation to network-scale settings.

Within the physics-informed traffic literature, domain decomposition has received limited attention. Usama et al. (2022) extended PINNs to traffic networks by decomposing a network into individual links and enforcing flow conservation constraints at junctions. While this is the closest prior work to decomposition in traffic PINNs, the decomposition is topology-driven, one sub-network per road link, rather than residual-guided, and it does not address adaptive subdomain discovery within a single freeway corridor. Huang

and Agarwal (2023) showed that physics-informed learning for the hyperbolic LWR equation yields substantially larger errors than for a diffusion-augmented counterpart when solutions contain shockwaves, establishing that the shockwave problem has measurable consequences for traffic estimation accuracy and motivating shock-oriented improvements beyond standard single-domain formulations.

2.2. Physics-Informed Neural Networks: Training Challenges

Physics-informed machine learning has emerged as a paradigm for integrating governing equations with data-driven models (Karniadakis et al., 2021). The PINN framework, formalized by Raissi et al. (2019), showed that governing PDEs can serve as a strong inductive bias in small-data regimes by penalizing PDE residuals at collocation points alongside data-fitting objectives. Since then, the primary research challenge has shifted from formulation to trainability.

Spectral bias is one such difficulty: neural networks trained with gradient descent learn low-frequency components of the solution faster than high-frequency ones, leading PINNs to over-smooth sharp gradients and discontinuities (Tancik et al., 2020). Fourier feature embeddings, which project the low-dimensional input into a higher-dimensional sinusoidal space, have been shown to mitigate this bias by enabling the network to represent high-frequency content from early in training.

A second challenge is *gradient pathology* in the composite PINN loss. Wang et al. (2021) showed that imbalance among data, boundary, and PDE loss gradients can substantially slow or destabilize convergence. Krishnapriyan et al. (2021) demonstrated systematic PINN failures on convection-dominated and reaction-dominated PDEs, arguing that soft PDE regularization can become ineffective on more challenging problems. Lei et al. (2025) recently formalized these failure modes specifically for traffic flow, showing that PINNs can perform worse than both their data-driven and physics-based counterparts when spatiotemporal resolution is insufficient or when gradient imbalance is severe.

Several remedies have been proposed. Wang et al. (2024) introduced causal training, which respects the temporal structure of time-dependent PDEs by weighting PDE residuals according to their position in the causal sequence. Wu et al. (2023) developed residual-based adaptive refinement (RAR), which dynamically adds collocation points in high-error regions. Self-adaptive loss weighting (McClenny and Braga-Neto, 2023) treats loss

weights as learnable parameters, though the effectiveness of such schemes varies across problem settings (Lei et al., 2025). These remedies improve optimization within a single global network but do not resolve the structural incompatibility between pointwise residual minimization and discontinuous solutions of hyperbolic conservation laws. This limitation motivates domain decomposition approaches that reduce the complexity of local functions.

2.3. Domain Decomposition PINNs

Domain decomposition (DD) reduces the complexity that any single network must represent. By partitioning the spatiotemporal domain into smaller subdomains, each handled by a dedicated sub-network, DD-PINNs represent local features more accurately and enable parallel training.

Jagtap et al. (2020) introduced conservative PINNs (cPINNs), which decompose the domain spatially and enforce strong-form flux continuity across interfaces, making the method particularly well-suited to conservation laws. Jagtap and Karniadakis (2020) generalized this idea into the extended PINN (XPINN) framework, which supports arbitrary space-time decompositions with residual-based continuity at subdomain interfaces. We adopt XPINN as our DD-PINN baseline because it supports spatial, temporal, and space-time decomposition within a unified framework, enabling systematic comparison of decomposition directions. Shukla et al. (2021) developed a parallel implementation of cPINNs and XPINNs, clarifying the computational trade-offs: cPINNs are communication-efficient for spatial decomposition, while XPINNs are more flexible because they also support temporal splitting. Hu et al. (2021) analyzed when XPINNs improve generalization, showing that decomposition creates a tradeoff between simpler local functions and fewer samples per subdomain. Moseley et al. (2023) proposed finite basis PINNs (FBPINNs), which use overlapping subdomains with compact-support basis functions to improve scalability and reduce spectral bias. Hu et al. (2023) introduced augmented PINNs (APINNs), which employ a gating network to realize soft, trainable domain decomposition with flexible parameter sharing.

Prior DD-PINN frameworks and many subsequent variants still depend on user-designed or initialization-dependent decompositions. More recent adaptive approaches have begun to relax this assumption. Peng et al. (2025) proposed AS-PINNs, which adapt interface positions through adversarial interaction among subnetworks for discontinuous high-order equations. Si and Yan (2025) proposed IDPINN, which uses a coarse small-data PINN to initialize subdomain networks and augments interface smoothness losses. Luo et al.

(2025) introduced progressive domain decomposition (PDD), which segments the domain according to residual-loss dynamics and preserves successful local models. Botvinick-Greenhouse et al. (2025) developed AB-PINNs, which insert new basis subdomains in regions of high residual loss during training. However, these methods have been developed for generic PDE benchmarks rather than for sparse fixed-sensor traffic state estimation, and they do not examine the direction of decomposition under fixed-sensor observability. Their interface designs are also not tailored to LWR-based freeway estimation, where conservation and shock-prone transitions are central.

Thus, the remaining gap is the joint treatment of residual-guided subdomain discovery and the selection of decomposition directions for sparse fixed-sensor freeway TSE.

2.4. PINNs for Conservation Laws with Shockwaves

Hyperbolic conservation laws, such as the LWR, admit weak solutions with discontinuities (shockwaves), posing a fundamental challenge for PINNs that minimize a pointwise strong-form PDE residual. At a shock, the classical PDE residual is undefined because the solution gradient diverges, and neural networks, as continuous function approximators, cannot accurately represent the discontinuous solution.

Huang and Agarwal (2023) demonstrated this difficulty explicitly for traffic, showing that physics-informed learning on the first-order hyperbolic LWR equation produces substantially larger errors than on a diffusion-augmented counterpart when solutions are non-smooth. This finding provides the most direct traffic-specific motivation for the present work. Several lines of research have sought to address the shockwave challenge. Coutinho et al. (2023) added adaptive localized artificial viscosity to stabilize PINNs near shocks, trading physical fidelity for numerical tractability. De Ryck et al. (2024) proposed weak PINNs (wPINNs), which replace the strong-form residual with a weak formulation suited to entropy solutions of scalar conservation laws. Neelan et al. (2025) studied the gap between conservative and non-conservative PDE formulations in PINNs, clarifying when Rankine-Hugoniot conditions must be explicitly enforced. Lorin and Novruzi (2024) proposed a non-diffusive neural network method that constructs smooth local solutions in subdomains separated by discontinuity lines defined from Rankine-Hugoniot jump conditions, thereby learning the discontinuity geometry itself. For adaptive sampling, Lu et al. (2021) introduced RAR in the DeepXDE framework, and

Wu et al. (2023) showed that residual-based adaptive sampling significantly improves accuracy near shocks compared to static collocation.

Most shock-oriented PINN remedies remain single-formulation methods based on viscosity, weak losses, or adaptive sampling, whereas explicit discontinuity-tracking methods such as NDNN learn the discontinuity geometry itself. ADD-PINN does not attempt to track the moving shock manifold directly; instead, it uses residual-guided spatial decomposition to isolate shock-prone transition regions into separate subdomains and applies conservation-aware interface constraints across fixed artificial interfaces. This positioning is intentionally different from wPINNs and NDNN: rather than reformulating the loss in weak form or explicitly learning discontinuity lines, ADD-PINN localizes difficult regions and reduces the complexity of local approximations within a traffic estimation workflow. Such a residual-guided strategy combining split placement, conservation-aware fixed-interface coupling, and coarse-to-fine warm-start training has not been explicitly developed for sparse fixed-sensor TSE.

In summary, the reviewed literature identifies four challenges for sparse, fixed-sensor freeway TSE. Adaptive decompositions should be driven by residual evidence from the traffic estimation problem itself; the decomposition direction should be matched to fixed-sensor observability, and coarse-to-fine warm starts remain underdeveloped for traffic DD-PINNs. Multi-day real-world validation with statistical testing is also needed to distinguish systematic gains from dataset-specific or seed-specific effects.

3. Methodology

This section presents the ADD-PINN framework for traffic state estimation, illustrated in Figure 2. We first formulate the problem (Section 3.1), then describe the network architecture (Section 3.2), loss function (Section 3.3), two-stage training framework (Section 3.4), adaptive subdomain detection (Section 3.5), interface conditions (Section 3.6), additional training components (Section 3.7), and decomposition direction analysis (Section 3.8).

3.1. Problem Formulation

We consider the problem of reconstructing the complete speed field $u(x, t)$ across a freeway segment from sparse fixed-sensor observations. This is a PDE-constrained state reconstruction (data assimilation) problem: unlike classical forward problems, no initial or boundary conditions are specified;

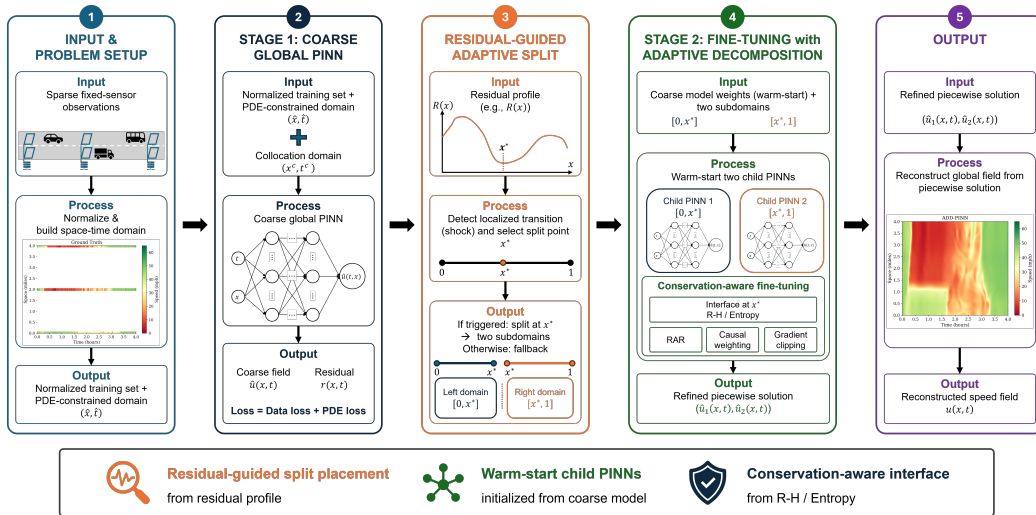


Figure 2: Framework overview of ADD-PINN.

unlike classical inverse problems, no PDE parameters are inferred. The free-flow speed v_f is pre-estimated from the data and held fixed throughout training.

Let $\Omega = [x_{\min}, x_{\max}] \times [0, T]$ denote the spatiotemporal domain. Traffic dynamics are governed by the Lighthill-Whitham-Richards (LWR) conservation law (Lighthill and Whitham, 1955; Richards, 1956):

$$\frac{\partial \rho}{\partial t} + \frac{\partial q(\rho)}{\partial x} = 0, \quad (1)$$

where $\rho(x, t)$ is the traffic density and $q(\rho)$ is the flow. In this study, we close Equation 1 with the Greenshields fundamental diagram (Greenshields et al., 1935):

$$q(\rho) = v_f \rho \left(1 - \frac{\rho}{\rho_{\text{jam}}} \right), \quad (2)$$

with v_f the free-flow speed and ρ_{jam} the jam density. This choice should be interpreted as one admissible first-order closure rather than a defining feature of ADD-PINN. Triangular diagrams are a standard alternative in freeway kinematic-wave modeling (Newell, 1993b). We use Greenshields here because its smooth, single-valued, differentiable form yields the speed-form residual in Equation 3 without piecewise branches or a min operator. A triangular or calibrated closure would require replacing the smooth residual and the

interface flux or characteristic terms with the corresponding piecewise or min-operator expressions. The residual-guided split detection and parent-to-child warm start do not depend on the parabolic form of Equation 2, because they operate on residual evaluations and network weights. Using the relation $u = v_f(1 - \rho/\rho_{\text{jam}})$, the conservation law can be rewritten in speed form:

$$\frac{\partial u}{\partial t} + (2u - v_f)\frac{\partial u}{\partial x} = 0. \quad (3)$$

Both speed and spatial/temporal coordinates are normalized to $[0, 1]$ via min-max scaling before being input to the neural network:

$$\hat{x} = \frac{x - x_{\min}}{x_{\max} - x_{\min}}, \quad \hat{t} = \frac{t}{T}, \quad \hat{u} = \frac{u - u_{\min}}{u_{\max} - u_{\min}}, \quad (4)$$

where u_{\min} and u_{\max} are the observed minimum and maximum speeds. All subsequent equations in Sections 3.2 to 3.8 operate in normalized coordinates unless otherwise noted. In this system, $\rho_{\text{jam}} = u_{\max} = 1$. We work consistently in these normalized coordinates throughout training, so the normalized density $\hat{\rho} = 1 - \hat{u}$ used in Section 3.6 is a normalized analog of the physical density rather than the physical density; the Rankine-Hugoniot and entropy interface losses are therefore conservation-aware regularizers in normalized coordinates rather than exact mass-conservation statements in physical units. Conversion to physical units uses $u = u_{\min} + \hat{u}(u_{\max} - u_{\min})$ and the corresponding flux scaling. After normalization, the PDE residual takes the form

$$r(x, t) = \frac{A \frac{\partial \hat{u}}{\partial x} - B \hat{u} \frac{\partial \hat{u}}{\partial x} - \frac{\partial \hat{u}}{\partial t}}{\sqrt{A^2 + B^2 + 1}}, \quad (5)$$

where $\hat{u}(x, t; \theta)$ is the network prediction in normalized coordinates and the coefficients are derived from the normalization:

$$C = c_{\text{fps}} \cdot \frac{T_{\text{range}}}{X_{\text{range}}}, \quad A = (v_f - 2u_{\min}) \cdot C, \quad B = 2(u_{\max} - u_{\min}) \cdot C. \quad (6)$$

Here, $c_{\text{fps}} = 5280/3600$ converts miles per hour to feet per second, T_{range} and X_{range} are the temporal and spatial extents of the domain in seconds and feet respectively, and u_{\min}, u_{\max} are the minimum and maximum observed speeds. The denominator $\sqrt{A^2 + B^2 + 1}$ normalizes the residual to $\mathcal{O}(1)$ regardless of the physical units and domain aspect ratio, which improves training stability by making the PDE loss comparable in magnitude to the data loss.

A set of N_{data} sensor observations $\mathcal{O} = \{(x_i^d, t_i^d, u_i^{\text{obs}})\}_{i=1}^{N_{\text{data}}}$ is available from fixed-location detectors at interior spatial positions. The TSE problem is formulated as the following optimization:

$$\theta^* = \arg \min_{\theta} \mathcal{L}_{\text{total}}(\theta), \quad (7)$$

where the total loss $\mathcal{L}_{\text{total}}$ is defined in Section 3.3. The formulation assumes a single connected freeway corridor without on-ramp or off-ramp source terms and uses lane-aggregated traffic states. These assumptions define the scope of the present evaluation and keep the comparison focused on domain decomposition rather than on traffic-model complexity. This formulation differs from classical forward PDE problems, which seek to propagate a solution from prescribed initial and boundary conditions, and from inverse problems, which seek to infer unknown PDE parameters from observations. Here, neither initial/boundary conditions nor PDE parameters are unknown: the free-flow speed v_f is pre-estimated and fixed, and the network must reconstruct the interior speed field solely from sparse sensor data and the PDE constraint. Because no initial or boundary conditions are imposed, the problem is not classically well-posed. In our offline reconstruction setting, observability is provided by full-window time series at each interior sensor, combined with the LWR residual, which together constrain the interior speed field through both data fitting and the PDE’s characteristic structure.

3.2. Network Architecture

Each subdomain Ω_s is assigned a dedicated feedforward neural network $\text{NN}_s(x, t; \theta_s)$. The normalized input coordinates (x, t) first pass through a Fourier feature mapping (Tancik et al., 2020):

$$\gamma(x, t) = [\sin(\mathbf{W}[x, t]^\top), \cos(\mathbf{W}[x, t]^\top)] \in \mathbb{R}^{2d_e}, \quad (8)$$

where $\mathbf{W} \in \mathbb{R}^{d_e \times 2}$ is a random matrix drawn from $\mathcal{N}(0, \sigma^2)$ with $\sigma = 10$ at initialization and held fixed thereafter. The embedding dimension d_e is set to half the first hidden layer width: for a first hidden layer of 256 neurons, $d_e = 128$, producing a 256-dimensional Fourier embedding. This mapping projects the two-dimensional input into a higher-dimensional space of sinusoidal features, enabling the network to learn high-frequency components otherwise suppressed by spectral bias.

The Fourier features feed into a sequence of fully connected hidden layers with tanh activations, followed by a linear output layer that produces a

single scalar: the predicted speed. The tanh activation is used because its smoothness keeps the derivatives required by the PDE residual continuous. Prior to domain decomposition, the parent network uses the architecture [2, 256, 128, 128, 128, 1], where the first dimension denotes the raw input size before Fourier embedding and the subsequent dimensions are the widths of the hidden and output layers. After decomposition, each child network uses [2, 256, 128, 128, 1], reducing the depth by one hidden layer to balance expressiveness with computational cost while retaining the same Fourier embedding dimension.

The layer counts should be interpreted as fixed implementation hyperparameters rather than calibrated optima. Single-domain methods use the parent architecture, while decomposed methods use the child architecture specified above. The child network is one hidden layer shallower than the parent to reduce per-subdomain cost after parent-to-child warm start while preserving the 256-dimensional Fourier embedding. This architectural convention, together with the total number of training epochs, initial collocation budget, optimizer, and loss weights, is shared by ADD-PINN and the baselines, as described in Section 4.2. The full settings are reported in Table 3. Therefore, the chosen layer count does not confer a method-specific architectural advantage on ADD-PINN.

The global solution is defined in a piecewise manner:

$$\hat{u}(x, t; \theta) = \sum_{s=1}^n \mathbf{1}_{\Omega_s}(x, t) \hat{u}_s(x, t; \theta_s), \quad (9)$$

where n is the number of subdomains and $\mathbf{1}_{\Omega_s}$ is the indicator function. Each point in the domain is handled by exactly one sub-network, permitting sharp transitions at subdomain interfaces when physically warranted (e.g., at shockwave locations).

3.3. Loss Function

The training objective is a weighted sum of three terms:

$$\mathcal{L}_{\text{total}}(\theta) = w_{\text{data}} \mathcal{L}_{\text{data}}(\theta) + w_{\text{pde}} \mathcal{L}_{\text{pde}}(\theta) + w_{\text{int}} \mathcal{L}_{\text{int}}(\theta), \quad (10)$$

with fixed weights $w_{\text{data}} = 0.85$, $w_{\text{pde}} = 0.05$, and $w_{\text{int}} = 0.10$, which are held constant across datasets, baselines, and seeds.

The **data loss** measures the mean squared error between predictions and sensor observations:

$$\mathcal{L}_{\text{data}}(\theta) = \frac{1}{N_{\text{data}}} \sum_{i=1}^{N_{\text{data}}} (\hat{u}(x_i^d, t_i^d; \theta) - u_i^{\text{obs}})^2. \quad (11)$$

The **PDE loss** penalizes violations of the LWR equation at collocation points sampled throughout Ω . When multiple subdomains are present, the PDE loss is computed in each subdomain and averaged:

$$\mathcal{L}_{\text{pde}}(\theta) = \frac{1}{n} \sum_{s=1}^n \frac{1}{N_{\text{pde}}^s} \sum_{j=1}^{N_{\text{pde}}^s} w_j^{\text{causal}} (r(x_j^c, t_j^c; \theta_s))^2, \quad (12)$$

where $r(\cdot)$ is the normalized residual from Equation (5). The causal weights w_j^{causal} are constant within each temporal bin and are defined in Section 3.7. The **interface loss** \mathcal{L}_{int} enforces consistency between adjacent subdomains and is defined in Section 3.6. Prior to decomposition (Stage 1), $\mathcal{L}_{\text{int}} = 0$ since only a single subdomain exists.

The weight $w_{\text{data}} = 0.85$ reflects the dominance of data fidelity in this data assimilation setting: sensor observations provide direct evidence of the traffic state, while the PDE serves as a regularizer that propagates information to unobserved regions. The relatively small $w_{\text{pde}} = 0.05$ prevents the physics loss from overwhelming the data loss, consistent with the findings of Lei et al. (2025) that excessive physics weighting can cause PINNs to fail for traffic flow estimation.

3.4. Two-Stage Training Framework

ADD-PINN employs a two-stage training procedure that separates coarse global learning (Stage 1) from fine-grained local refinement (Stage 2). Between these two training stages, a single transition step performs shock screening and residual analysis to determine whether decomposition is used and, when it is used, where the spatial split is placed. This two-stage structure with a residual-guided transition is the core methodological contribution (C1).

Stage 1: Coarse PINN (epochs 1 to E_{split}). A single neural network is trained on the full domain Ω , identically to a standard (vanilla) PINN except that

causal weighting (Section 3.7) is applied to the PDE loss. The Adam optimizer (Kingma and Ba, 2014) is used with a learning rate of 10^{-3} . During Stage 1, domain decomposition, residual-adaptive refinement (RAR), and interface conditions are all disabled. Stage 1 is used to produce an approximate solution whose PDE residual reveals the spatial structure of shock-prone transition regions, rather than to serve as the final estimator. In our experiments, $E_{\text{split}} = 5,000$ epochs.

Decomposition step: Residual analysis and adaptive splitting. At epoch E_{split} , the coarse PINN solution is analyzed to determine whether and where the domain should be partitioned. First, a data-driven shock indicator is computed from the observed sensor data to assess whether the traffic scenario contains localized features (shockwaves) that would benefit from decomposition. Given sensor observations $\mathcal{O} = \{(x_i, t_k, u_{i,k})\}$, we compute per-pair mean spatial gradients g_i^x over timestamps common to adjacent sensors i and $i+1$, and per-sensor mean temporal gradients g_i^t from consecutive samples at sensor i . The shock indicator is the dimensionless max-to-mean ratio of these gradients,

$$\mathcal{S}(\mathcal{O}) = \max \left\{ \frac{\max_i g_i^x}{g^x + \varepsilon}, \frac{\max_i g_i^t}{g^t + \varepsilon} \right\}, \quad \varepsilon = 10^{-10}, \quad (13)$$

and decomposition is enabled if and only if $\mathcal{S}(\mathcal{O}) > \tau_{\text{shock}}$, with $\tau_{\text{shock}} = 2.0$ throughout (Table 3). Because \mathcal{S} is invariant to a global rescaling of u , the threshold has a direct interpretation: it requires the steepest local gradient to be at least twice the field’s average gradient before any subdomain interface is introduced. The threshold is used as a fixed protocol choice across all experiments rather than as an optimized deployment parameter, so sensitivity across corridors and sensing regimes is left to future work. If a shock is detected, the spatial residual profile of the coarse PINN is analyzed to determine split positions via the adaptive procedure described in Section 3.5. We distinguish two operating modes within the same ADD-PINN framework. In the default shock-screened mode, decomposition is activated only when $\mathcal{S}(\mathcal{O}) > \tau_{\text{shock}}$; otherwise, the single coarse network continues into Stage 2 as the fallback estimator. In the decomposition-enabled mode, used for the primary I-24 comparison because the selected days contain clear transition structure, the split/no-split decision is fixed while split locations are still selected from the residual profile. Thus, the I-24 results evaluate residual-guided spatial decomposition under transition-rich conditions, whereas the

NGSIM analysis in Section 5.5 evaluates the shock-screened fallback. When decomposition is used, child networks are created and initialized from the parent weights as described in Section 3.5; otherwise, the single-domain fallback proceeds to Stage 2 without interface losses.

Stage 2: Fine-tuning after the transition step (epochs $E_{\text{split}} + 1$ to E_{max}). After decomposition, all subdomain networks are trained simultaneously with the following enhancements over Stage 1:

- *Reduced learning rate:* Adam with $\text{lr} = 10^{-4}$ and a step decay schedule (factor 0.9 every 5,000 epochs).
- *Interface conditions:* Rankine-Hugoniot and entropy constraints are enforced at subdomain boundaries (Section 3.6).
- *Residual-adaptive refinement:* Collocation points are periodically added in high-residual regions (Section 3.7).
- *Causal weighting:* The PDE loss applies temporal weighting that emphasizes earlier time steps (Section 3.7).
- *Gradient clipping:* Gradient norms are clipped to a maximum of 5.0 to prevent training instabilities after decomposition.

In our experiments, $E_{\text{max}} = 20,000$ epochs, so Stage 2 runs for 15,000 epochs. No further domain splits occur during Stage 2. Appendix D provides the full training pseudocode.

3.5. Adaptive Subdomain Detection

At epoch E_{split} , ADD-PINN analyzes the spatial distribution of the PDE residual to compute candidate split positions for the decomposition-enabled stage. In the default shock-screened mode, this residual-guided split placement is preceded by the fallback decision in Section 3.4. Thus, the method reduces manual specification of split locations when decomposition is used, while allowing the full algorithm to retain a single-domain model when localized transition evidence is weak.

1. **Residual evaluation.** The normalized PDE residual $r(x, t)$ from Equation (5) is evaluated on a uniform grid of $n_x \times n_t$ points ($n_x = 200$, $n_t = 100$) spanning the full domain.

2. **Spatial residual profile.** The squared residual is averaged over the temporal dimension to obtain a one-dimensional spatial profile:

$$R(x) = \frac{1}{n_t} \sum_{j=1}^{n_t} r(x, t_j)^2. \quad (14)$$

Peaks in $R(x)$ indicate spatial locations where the coarse PINN has the highest PDE error, typically corresponding to shockwave fronts or regions of rapid spatial variation.

3. **Smoothing.** A moving average filter with kernel size $K = \max(3, \lfloor n_x/20 \rfloor)$ (enforced to be odd) is applied to $R(x)$ to suppress noise and ensure robust peak detection.
4. **Peak detection.** Local maxima of the smoothed profile that exceed 30% of the global maximum are identified, subject to a minimum inter-peak distance of 10% of n_x grid points. The outermost 10% of the domain on each side is excluded from the peak search to avoid boundary artifacts. The number of detected peaks determines the number of subdomains: k peaks yield $k + 1$ candidate subdomains.
5. **Valley detection and split positioning.** All local minima in the smoothed profile are identified. The k deepest minima (those with the smallest $R(x)$ values) are selected as split positions. Placing boundaries in low-residual valleys avoids splitting a shockwave in half, which would complicate interface enforcement. This heuristic is most effective when shockwave positions are relatively stationary over the observation window; for rapidly moving shocks, temporal averaging of the residual may reduce localization precision. If fewer minima exist than required, equally spaced splits are used as a fallback. Split positions are validated to maintain a minimum spacing $\delta_{x,\min}$ from domain edges and from each other.
6. **Child network creation and initialization.** The domain is partitioned at the validated split positions. For each child subdomain Ω_s , a new network NN_s is created. If the child architecture differs from the parent (fewer hidden layers), compatible layers are copied directly; otherwise, the full parent state is loaded. Each child network then undergoes 200 additional initialization epochs in which it is trained (via Adam, lr = 10^{-3}) to match the parent network’s output at 2,000 random points within its subdomain. This ensures that the piecewise solu-

tion immediately after decomposition closely approximates the coarse PINN solution, providing a smooth warm start for Stage 2.

This procedure performs spatial decomposition based on the time-averaged residual profile $R(x)$, the default decomposition direction evaluated in Section 3.8. The same residual-averaging procedure is used for the other decomposition directions in the ablation study of Section 5.2. For temporal decomposition, the analogous profile $R(t) = (1/n_x) \sum_i r(x_i, t)^2$ is computed by averaging the squared residual over the spatial dimension, and split positions in time are identified at residual valleys using the same peak and valley detection logic. For space-time decomposition, both $R(x)$ and $R(t)$ are computed independently, and their respective valley positions are used jointly to create a 2×2 subdomain partition. Interface treatment is assigned by decomposition direction, as detailed in Section 3.6.

3.6. Interface Conditions

At each spatial interface x_{int} between adjacent subdomains Ω_L and Ω_R , ADD-PINN applies conservation-aware interface constraints. Let $\hat{u}_L(t) = \hat{u}_L(x_{\text{int}}^-, t)$ and $\hat{u}_R(t) = \hat{u}_R(x_{\text{int}}^+, t)$ denote the left and right predictions at the interface, evaluated at $N_{\text{int}} = 200$ random time samples per training step.

Each interface is classified as either *shock* or *smooth* based on the mean density jump. Let $\hat{\rho}_L$ and $\hat{\rho}_R$ be the densities obtained from the predicted speeds via $\hat{\rho} = \rho_{\text{jam}}(1 - \hat{u}/u_{\text{max}})$, where ρ_{jam} and u_{max} both equal 1 in the normalized coordinate system. If the mean absolute density jump $|\overline{\hat{\rho}_L - \hat{\rho}_R}|$ exceeds a threshold δ_{shock} , the interface is classified as a shock; otherwise, it is treated as smooth.

Smooth interface: C^0/C^1 continuity. When no shock is present, the solution should be smooth across the interface. The loss enforces both value and gradient continuity:

$$\mathcal{L}_{\text{smooth}} = \frac{1}{N_{\text{int}}} \sum_{m=1}^{N_{\text{int}}} (\hat{u}_L(t_m) - \hat{u}_R(t_m))^2 + \frac{1}{N_{\text{int}}} \sum_{m=1}^{N_{\text{int}}} (\partial_x \hat{u}_L(t_m) - \partial_x \hat{u}_R(t_m))^2. \quad (15)$$

Before specifying the interface loss, we clarify the intended role of these fixed interfaces. ADD-PINN's subdomain boundaries are artificial fixed spatial interfaces, not parameterizations of the true moving shock trajectory. The Rankine-Hugoniot and entropy terms introduced below are

conservation-aware regularizers that discourage nonphysical mass imbalance across these fixed artificial interfaces, functioning as a shock-localization strategy rather than an exact discontinuity-tracking method such as that of Lorin and Novruzi (2024). Applications requiring exact shock geometry are better served by weak-form or explicit discontinuity-line formulations (De Ryck et al., 2024; Lorin and Novruzi, 2024; Neelan et al., 2025); the present formulation trades that rigor for simplicity of integration with sparse fixed-sensor data and automatic differentiation.

Shock interface: Rankine-Hugoniot and entropy conditions. When a shock is detected, enforcing C^0/C^1 continuity would be physically incorrect because the LWR solution is discontinuous at the shock. Instead, we impose the Rankine-Hugoniot (R-H) condition (Rankine, 1870; Hugoniot, 1887), which ensures conservation of vehicles across the discontinuity. We introduce a trainable shock speed s for each interface and penalize deviations from the R-H relation:

$$\mathcal{L}_{\text{RH}} = \frac{1}{N_{\text{int}}} \sum_{m=1}^{N_{\text{int}}} \left[s(\hat{\rho}_L(t_m) - \hat{\rho}_R(t_m)) - (q(\hat{\rho}_L(t_m)) - q(\hat{\rho}_R(t_m))) \right]^2. \quad (16)$$

The shock speed s is initialized to zero and updated via stochastic gradient descent with a learning rate of 10^{-3} .

To select the physically admissible (entropy) solution among possible weak solutions, we additionally enforce the Lax entropy condition, $\lambda(\hat{\rho}_L) \geq s \geq \lambda(\hat{\rho}_R)$, where $\lambda(\rho) = dq/d\rho = u_{\text{max}}(1 - 2\rho/\rho_{\text{jam}})$ is the characteristic speed:

$$\mathcal{L}_{\text{entropy}} = \frac{1}{N_{\text{int}}} \sum_{m=1}^{N_{\text{int}}} \left[\text{ReLU}(s - \lambda(\hat{\rho}_L(t_m)))^2 + \text{ReLU}(\lambda(\hat{\rho}_R(t_m)) - s)^2 \right]. \quad (17)$$

This condition requires that characteristics propagate *into* the shock from both sides. The total shock interface loss is $\mathcal{L}_{\text{shock}} = \mathcal{L}_{\text{RH}} + w_{\text{entropy}} \mathcal{L}_{\text{entropy}}$, where $w_{\text{entropy}} = 1.0$.

The overall interface loss selects between the two modes based on the classified interface type:

$$\mathcal{L}_{\text{int}} = \sum_{\text{interfaces}} \begin{cases} \mathcal{L}_{\text{shock}} & \text{if } |\overline{\hat{\rho}_L - \hat{\rho}_R}| > \delta_{\text{shock}}, \\ \mathcal{L}_{\text{smooth}} & \text{otherwise.} \end{cases} \quad (18)$$

The interface conditions defined above contrast with XPINN’s residual-based continuity (Jagtap and Karniadakis, 2020), which does not explicitly encode the R-H conservation relation. For the temporal and space-time ablations (Section 5.2), spatial sub-interfaces use the same R-H treatment, whereas temporal sub-interfaces enforce C^0 solution continuity, $\mathcal{L}_{\text{cont},t} = (1/N_{\text{int}}) \sum_m [\hat{u}_{\text{after}}(x_m, t^*) - \hat{u}_{\text{before}}(x_m, t^*)]^2$, because the R-H relation is a spatial shock condition.

3.7. Additional Training Components

Residual-adaptive refinement (RAR). During Stage 2, additional collocation points are periodically injected in high-residual regions to concentrate training effort near shockwaves (Wu et al., 2023). Every 2,500 epochs, 5,000 candidate points are sampled uniformly in each subdomain, the absolute PDE residual is evaluated at each candidate, and the 2,500 points with the largest $|r|$ are added to the collocation set. This targeted refinement is particularly effective near subdomain interfaces and shock fronts, where residuals tend to be largest.

Causal weighting. The PDE loss applies a temporal weighting scheme inspired by Wang et al. (2024) that assigns a higher weight to earlier time steps throughout training (both Stage 1 and Stage 2). The rationale is that PDE solutions should be solved sequentially in time: errors at early times propagate forward, so the network should prioritize accuracy at earlier times. Concretely, the collocation points are sorted by their temporal coordinate and partitioned into n_{bins} equal-sized bins. The causal weight for bin j is

$$w_j^{\text{causal}} = \exp\left(-\epsilon \sum_{k < j} \bar{r}_k^2\right), \quad (19)$$

where \bar{r}_k^2 is the mean squared residual in bin k and ϵ is a causality parameter. The weights are detached from the computational graph (treated as constants during backpropagation) so that gradients flow only through the residuals, not through the weighting scheme.

Gradient clipping. All parameter gradients are clipped to a maximum norm of 5.0 at every training step. This prevents training instabilities caused by large gradients that can arise immediately after domain decomposition, when the interface loss introduces new terms into the objective.

3.8. Decomposition Direction Analysis

Although the ADD-PINN framework can decompose the domain along any combination of spatial and temporal dimensions, we use spatial-only decomposition as the default for fixed-sensor TSE in the evaluated settings and evaluate this choice empirically in Section 5.2. Three arguments support this design choice.

Argument 1: Shockwave geometry. Shockwaves in LWR traffic flow manifest primarily as spatially localized transition regions: at any given time, the speed field exhibits a sharp gradient across a congestion boundary in the x -direction. In our fixed-sensor, lane-aggregated, finite-resolution setting, the corresponding temporal speed trace at a given sensor location typically varies more gradually than the spatial profile across the transition. Spatial decomposition places subdomain interfaces near these localized transitions, directly addressing the dominant source of approximation difficulty. Temporal decomposition would split the domain along a direction where the aggregated signal is comparatively smoother, offering less benefit for transition-region resolution.

Argument 2: Data coverage asymmetry. Fixed sensors provide fundamentally asymmetric coverage of the spatiotemporal domain. In the spatial direction, sensors occupy only a small fraction of the domain (e.g., 5 sensors covering 5 out of 100 spatial cells, or 5% spatial coverage). In the temporal direction, each sensor records a continuous time series spanning the entire observation period (effectively 100% temporal coverage). Domain decomposition is most beneficial where observations are sparse: spatial decomposition reduces the unsupervised gap between sensors by assigning dedicated networks to each inter-sensor region.

Argument 3: Residual anisotropy. For first-order hyperbolic conservation laws such as LWR, the PDE residual of a smooth approximation concentrates spatially near discontinuities (shockwaves) while remaining relatively uniform in time. Empirically, for the coarse PINN approximations we observe, large PDE residuals concentrate near shock-prone spatial locations, while the residual’s temporal profile remains comparatively flat. This pattern reflects the combination of shockwave geometry and the lane-aggregated finite-resolution observation grid used in our experiments rather than an exact property of LWR weak solutions. Consequently, the spatial residual profile $R(x)$ (Equation (14)) exhibits pronounced peaks near shockwaves, while

the corresponding temporal profile $R(t)$ remains comparatively flat across all ablation configurations. In the evaluated cases, the dominant source of approximation error is spatial, making spatial decomposition an efficient allocation of additional modeling capacity. The empirical comparison of $R(x)$ and $R(t)$ across multiple datasets is presented in Section 5.2.

We note that temporal decomposition may be beneficial in other TSE contexts, such as probe-vehicle-based estimation, where spatial coverage is dense but temporal sampling is sparse. Evaluating such settings is outside the scope of the present study.

4. Experimental Setup

4.1. Datasets

The empirical evaluation uses two trajectory datasets, each with a distinct role. The I-24 MOTION dataset serves as the primary benchmark for evaluating ADD-PINN under sparse fixed-sensor reconstruction with localized congestion and shock-prone transition regions. The NGSIM I-80 dataset is used as a supplementary negative-control case to test whether the proposed shock indicator can suppress domain decomposition when the traffic field does not contain a clearly localized transition boundary. The data collection sites are shown in Figure B.7.

I-24 MOTION. We evaluate ADD-PINN on five days of the I-24 MOTION dataset (Gloude-mans et al., 2023), which captures lane-level vehicle trajectories along a 4.2-mile (21,120 ft) corridor of Interstate 24 near Nashville, Tennessee, using 276 overhead cameras at approximately 2-second resolution. The raw trajectory data are aggregated into a spatiotemporal grid of 100 spatial cells ($\Delta x \approx 211$ ft) and 7,200 time steps ($\Delta t = 2$ s), covering a 4-hour observation window from 06:00 to 10:00 CST. The five days span a range of traffic conditions, from mild free-flow to severe incident-induced congestion, as summarized in Table 1. This diversity enables the primary evaluation of ADD-PINN under both recurrent and non-recurrent congestion on a long freeway corridor.

NGSIM I-80. We additionally use the NGSIM I-80 trajectory dataset as a supplementary negative-control case (USDOT, 2016; Huang and Agarwal, 2022). The dataset contains detailed vehicle trajectories collected from a 1,600-ft segment of the I-80 freeway in Emeryville, California. Following

Table 1: Summary of the primary I-24 MOTION datasets. All I-24 datasets span a 4-hour window from 06:00 to 10:00 CST. The congestion ratio is defined as the percentage of spatiotemporal cells in which the observed speed is below 45 mph.

Date	Day	Traffic condition	Cong. (%)
2022-11-21	Mon	Rear-end collision WB near MM 59.7; congestion 06:14-07:43	55
2022-11-22	Tue	No incidents; typical weekday recurrent congestion	47
2022-11-23	Wed	Sideswipe WB lane 1 at MM 59.2; congestion 07:35-07:45	11
2022-11-29	Tue	No incidents; severe recurrent congestion	63
2022-12-02	Fri	Two-vehicle crash WB near MM 61.8; 07:38-08:20	37

prior traffic PINN studies, we use the 15-min PM peak interval from 16:00 to 16:15 on April 13, 2005 and aggregate the speed field using a spatial resolution of $\Delta x = 20$ ft and a temporal resolution of $\Delta t = 5$ s. Unlike the I-24 MOTION cases, this short segment exhibits diffuse congestion without a clearly localized transition boundary in the selected interval. Therefore, NGSIM is not used as the primary evidence for decomposition accuracy. Instead, it is used to test the regime-adaptive behavior of ADD-PINN, namely whether the default shock indicator can retain the single-domain fallback when the evidence for domain decomposition is weak. The same sensor counts, $n_s \in \{3, 4, 5, 6, 7\}$, ten random seeds, and relative L_2 error metric are used for the NGSIM supplementary experiment.

Speed values are normalized to $[0, 1]$ via min-max scaling: $\hat{u} = (u - u_{\min}) / (u_{\max} - u_{\min})$, where u_{\min} and u_{\max} are computed from the full trajectory-derived aggregated speed field in each dataset. The free-flow speed v_f is estimated as the 95th percentile of the full aggregated field and held fixed throughout training. Because these statistics are derived from the full field rather than the sparse sensor subset, the present study should be read as an offline reconstruction evaluation. Online or streaming deployment would require these quantities to be estimated from sensor observations alone or from historical aggregates; we return to this point in Section 6.3. Given a domain discretized into N spatial cells, n_s sensors are placed at equally spaced *interior* positions by generating $n_s + 2$ equally spaced indices from 0 to $N - 1$ and discarding the two boundary indices. Formally, the candidate indices are $\text{linspace}(0, N - 1, n_s + 2)$, and the n_s interior elements (excluding the first and last) are retained and rounded to the nearest integer. For example, with $n_s = 5$, the sensor cell indices are approximately $\{16, 33, 49, 66, 82\}$ for I-24 MOTION ($N = 100$) and

{13, 26, 40, 53, 66} for NGSIM I-80 ($N = 80$). These are virtual fixed sensors sampled from trajectory-derived aggregated fields rather than physical loop-detector records. This design enables controlled comparison across sensor counts and full-field error computation, but the evidence should be interpreted as offline reconstruction rather than online deployment.

4.2. Baseline Methods

We compare ADD-PINN (B6) against five baselines that represent a progression from data-driven to increasingly sophisticated physics-informed approaches. The benchmark isolates adaptive decomposition within neural and PINN-family estimators, consistent with recent PIDL traffic TSE studies in sparse-data settings (Shi et al., 2022; Zhang et al., 2024). It should not be interpreted as a claim of superiority over calibrated classical TSE methods, which require distinct calibration, observation-model, and deployment assumptions and are treated as a separate benchmark direction in Section 6.3. Table 2 summarizes the components present in each method.

Table 2: Component comparison of evaluated methods.

Component	B1 NN	B2 PINN	B3 RAR	B4 Visc.	B5 XPINN	B6 Ours
PDE constraint (LWR)		✓	✓	✓	✓	✓
Adaptive collocation (RAR)			✓			✓
Viscosity regularization				✓		
Domain decomposition					✓	✓
Adaptive decomposition						✓
Two-stage training						✓
R-H + entropy interface						✓
Causal weighting						✓
Parent weight initialization						✓

References: B2 Raissi et al. (2019); Huang and Agarwal (2022); B3 Wu et al. (2023); B4 Huang and Agarwal (2022, 2023); B5 Jagtap and Karniadakis (2020); B6 (ADD-PINN, this work).

- **B1 (Neural network).** A feedforward network with the same architecture as ADD-PINN’s parent, trained on sensor data only without any PDE constraint.
- **B2 (Vanilla PINN)** (Raissi et al., 2019; Huang and Agarwal, 2022). A standard PINN minimizing the weighted sum of data and PDE losses

with fixed weights ($w_{\text{data}} = 0.85$, $w_{\text{pde}} = 0.05$). No decomposition or adaptive refinement.

- **B3 (PINN + RAR)** (Wu et al., 2023). A vanilla PINN augmented with residual-adaptive refinement: every 2,500 epochs, 2,500 new collocation points are added in regions of high PDE residual. Isolates the effect of adaptive collocation from decomposition.
- **B4 (PINN + Viscosity)** (Huang and Agarwal, 2022, 2023). A PINN that adds an artificial viscosity term $\varepsilon \partial^2 u / \partial x^2$ (with $\varepsilon = 0.1$) to the LWR PDE, motivated by the finding that standard PINNs cannot accurately represent non-smooth LWR solutions (Huang and Agarwal, 2023).
- **B5 (XPINN)** (Jagtap and Karniadakis, 2020). The extended PINN framework with $n_x \times n_t = 2 \times 2 = 4$ space-time subdomains at equally spaced splits, each with the same child architecture as ADD-PINN ([2, 256, 128, 128, 1]). Interface coupling follows Jagtap and Karniadakis (2020) via residual continuity plus a solution-average penalty. Networks are initialized randomly without parent transfer and trained jointly from epoch 0 for the full 20,000 epochs. To ensure a fair comparison, XPINN uses the same loss weights as ADD-PINN ($w_{\text{data}} = 0.85$, $w_{\text{pde}} = 0.05$, $w_{\text{int}} = 0.10$), the same StepLR schedule, and the same gradient clipping. XPINN is used here as a standard fixed space-time DD-PINN baseline rather than as an optimized XPINN variant; the comparison therefore evaluates ADD-PINN as a coupled traffic-specific design, not the isolated effect of each individual component.

All methods follow the architecture convention specified in Section 3.2: single-domain methods use the parent architecture, while decomposed methods use the child architecture. They also share the same total number of training epochs, initial collocation budget, optimizer (Adam, initial learning rate of 10^{-3}), and loss weights. Method-specific enhancements (Stage 2 learning-rate reduction for ADD-PINN, StepLR for DD methods, RAR for B3 and B6) differ across methods.

4.3. Evaluation and Implementation

Each method is evaluated on all 5 I-24 datasets, each with 5 sensor configurations ($n_s \in \{3, 4, 5, 6, 7\}$) and 10 random seeds, yielding $5 \times 5 \times 10 = 250$

runs per method and $6 \times 250 = 1,500$ runs in total. Sensors are placed at equally spaced interior positions as described in Section 4.1.

The primary evaluation metric is the relative L_2 error (%), computed in physical speed units (mph) over all spatiotemporal grid points:

$$\text{Relative } L_2 \text{ Error} = \frac{\sqrt{\sum_j (u_{\text{mph}}^{\text{pred}}(x_j, t_j) - u_{\text{mph}}^{\text{true}}(x_j, t_j))^2}}{\sqrt{\sum_j (u_{\text{mph}}^{\text{true}}(x_j, t_j))^2}} \times 100\%. \quad (20)$$

For comparisons between ADD-PINN and each baseline, we report the win/loss record across all 25 configurations (5 datasets \times 5 sensor counts), where each configuration’s result is the mean over 10 seeds. Statistical significance is assessed using paired t -tests across configurations, and effect sizes are reported as Cohen’s d . A configuration is counted as a *win* for the method with the lower mean L_2 error.

All models are implemented in PyTorch and trained on a single NVIDIA RTX 3060 Ti GPU. Table 3 summarizes the hyperparameters for the I-24 MOTION experiments. For reproducibility, all random seeds are fixed at the beginning of each run, controlling the random number generators in PyTorch, NumPy, and CUDA. The 10 seeds listed in Table 3 are used consistently across all methods, datasets, and sensor configurations. Training time per run is approximately 500 seconds for ADD-PINN on the I-24 datasets. Reported training times correspond to wall-clock training time (forward/backward passes, RAR sampling, interface loss, and optimizer steps), averaged across 10 seeds per configuration; data preprocessing, evaluation, and visualization are excluded. All methods are run on the same NVIDIA RTX 3060 Ti GPU under the method-specific batching protocols reported in Tables 3 and 6.

5. Results

This section evaluates ADD-PINN on five I-24 MOTION days spanning accident, normal, mild, severe, and secondary accident conditions. The primary metric is the relative L_2 error, computed in physical speed units, over the entire space-time field. Section 5.1 reports the main comparison against all baselines. Section 5.2 examines decomposition direction. Section 5.3 analyzes sensitivity to sensor density. Section 5.4 compares computational cost, and Section 5.5 provides a supplementary negative control on NGSIM.

Table 3: Hyperparameters for I-24 MOTION experiments.

Parameter	Value
<i>Architecture</i>	
Parent / Child network	[2, 256, 128, 128, 128, 1] / [2, 256, 128, 128, 1]
Fourier embedding (d_e, σ)	128, 10.0; activation: tanh
<i>Training</i>	
Seeds	42, 123, 456, 789, 1024, 2048, 3000, 4096, 5555, 7777
Epochs (total / Stage 1)	20,000 / 5,000
Learning rate (Stage 1 / Stage 2)	10^{-3} / 10^{-4} (Adam); StepLR(5000, 0.9)
Batch size (data / collocation)	4,096 / $\max(512, 2048/n)$ per subdomain
Collocation points (N_{pde})	50,000 (LHS)
Gradient clipping	max norm = 5.0
$w_{\text{data}}, w_{\text{pde}}, w_{\text{int}}$ (fixed)	0.85, 0.05, 0.10
<i>Domain decomposition</i>	
Residual grid ($n_x \times n_t$)	200×100
Smoothing kernel	$\max(3, \lfloor n_x/20 \rfloor)$, odd
Peak threshold / min distance	30% of $\max R(x)$ / 10% of n_x
Min subdomain width ($\delta_{x,\text{min}}$)	0.15 (normalized)
Shock indicator	2.0
Child init (epochs / points)	200 / 2,000
<i>RAR (Stage 2 only)</i>	
Frequency / candidates / added	Every 2,500 epochs / 5,000 / 2,500
<i>Causal weighting</i>	
Temporal bins / ϵ	10 / 1.0
<i>Interface conditions</i>	
Points / δ_{shock} / w_{entropy}	200 / 0.1 / 1.0
Shock speed learning rate	10^{-3} (SGD)

5.1. Main Comparison on I-24 MOTION

Table 4 reports the primary I-24 results under the decomposition-enabled mode defined in Section 3.4, in which decomposition is fixed across all I-24 configurations while split positions are selected from the residual profile. The table reports the mean relative L_2 error for all 25 configurations, each averaged over 10 random seeds. ADD-PINN (B6) achieves the lowest error in 18 of 25 configurations, while XPINN (B5) is best in 6 and PINN+RAR (B3) is best in 1. The advantage of ADD-PINN is concentrated in the sparse regime. For $n_s \in \{3, 4, 5\}$, ADD-PINN ranks first in 14 of 15 configurations. These results indicate that residual-guided adaptive spatial decomposition is most beneficial when sparse fixed sensors leave large unobserved gaps and when the traffic field contains localized transition regions that are difficult for a single PINN to represent.

Pairwise statistical tests indicate that these gains are not driven by isolated configurations. Relative to XPINN, ADD-PINN reduces the mean relative L_2 error by 0.67 percentage points with a 95% confidence interval of [0.29, 1.04]. Relative to Vanilla PINN, the mean reduction is 1.49 percentage points with a 95% confidence interval of [1.15, 1.83]. All pairwise improvements remain significant after Holm-Bonferroni correction and are supported by nonparametric Wilcoxon signed-rank tests (Appendix C.1). In absolute terms, ADD-PINN achieves a mean root mean squared error (RMSE) of 5.60 mph across all I-24 configurations, compared to 6.10 mph for Vanilla PINN and 5.81 mph for XPINN. At the sparsest setting, $n_s = 3$, the RMSE improvement over Vanilla PINN is 0.78 mph (6.45 versus 7.22 mph), which provides practical context for the relative L_2 gains.

Averaged over sensor counts, ADD-PINN ranks first on four of the five I-24 days. Its largest average gain occurs on 20221129, the severe day with 63% congestion, where ADD-PINN records 21.88% relative L_2 error and improves on Vanilla PINN and XPINN by 1.85 and 1.01 percentage points, respectively. The smallest gain occurs on 20221123, the mild day with 11% congestion, where ADD-PINN records 9.79% and is effectively tied with XPINN, differing by only 0.03 percentage points. The accident days 20221121 and 20221202 exhibit similarly strong gains, with average improvements of 1.71 to 1.83 percentage points over Vanilla PINN and 0.69 to 0.96 percentage points over XPINN. The day-level pattern indicates that the benefit of ADD-PINN is associated less with congestion percentage alone than with the presence of localized transition regions that create concentrated reconstruction difficulty.

Table 4: Mean relative L_2 error (%) on I-24 MOTION datasets. Each entry is the mean over 10 random seeds. The lowest error in each row is shown in **bold**. B1: NN, B2: Vanilla PINN, B3: PINN+RAR, B4: PINN+Viscosity, B5: XPINN, B6: ADD-PINN (Ours).

Date	n_s	B1	B2	B3	B4	B5	B6
20221121	3	43.99	22.66	21.78	21.59	21.67	20.69
	4	37.28	17.86	17.03	16.75	16.76	15.84
	5	34.34	16.91	16.42	16.22	16.04	15.06
	6	32.21	16.24	16.01	15.71	15.57	15.09
	7	26.79	15.62	14.47	14.26	14.17	14.07
20221122	3	42.26	22.36	22.23	22.10	22.01	19.70
	4	38.30	20.08	19.46	19.54	19.26	17.92
	5	34.10	18.82	18.08	18.03	17.91	17.17
	6	31.13	17.10	16.43	16.32	16.23	16.48
	7	27.96	15.68	15.04	14.88	14.60	15.41
20221123	3	37.50	11.91	11.22	11.22	11.15	10.66
	4	30.52	10.73	10.30	10.28	10.15	10.19
	5	24.17	10.25	9.63	9.63	9.66	9.61
	6	23.07	9.96	9.39	9.48	9.43	9.58
	7	20.81	9.07	8.79	8.75	8.66	8.92
20221129	3	50.62	27.06	26.86	26.62	26.88	24.87
	4	47.31	25.79	25.12	25.15	25.09	23.54
	5	42.76	23.53	22.83	22.79	22.58	21.07
	6	39.02	22.02	21.22	21.15	20.97	20.38
	7	34.12	20.25	19.26	19.26	18.95	19.55
20221202	3	40.85	21.04	20.92	20.64	20.45	17.98
	4	38.76	19.02	18.56	18.55	18.35	16.84
	5	34.22	18.06	17.48	17.45	17.06	16.03
	6	29.90	16.70	16.01	15.93	15.66	15.30
	7	25.71	15.13	14.57	14.36	14.08	14.65

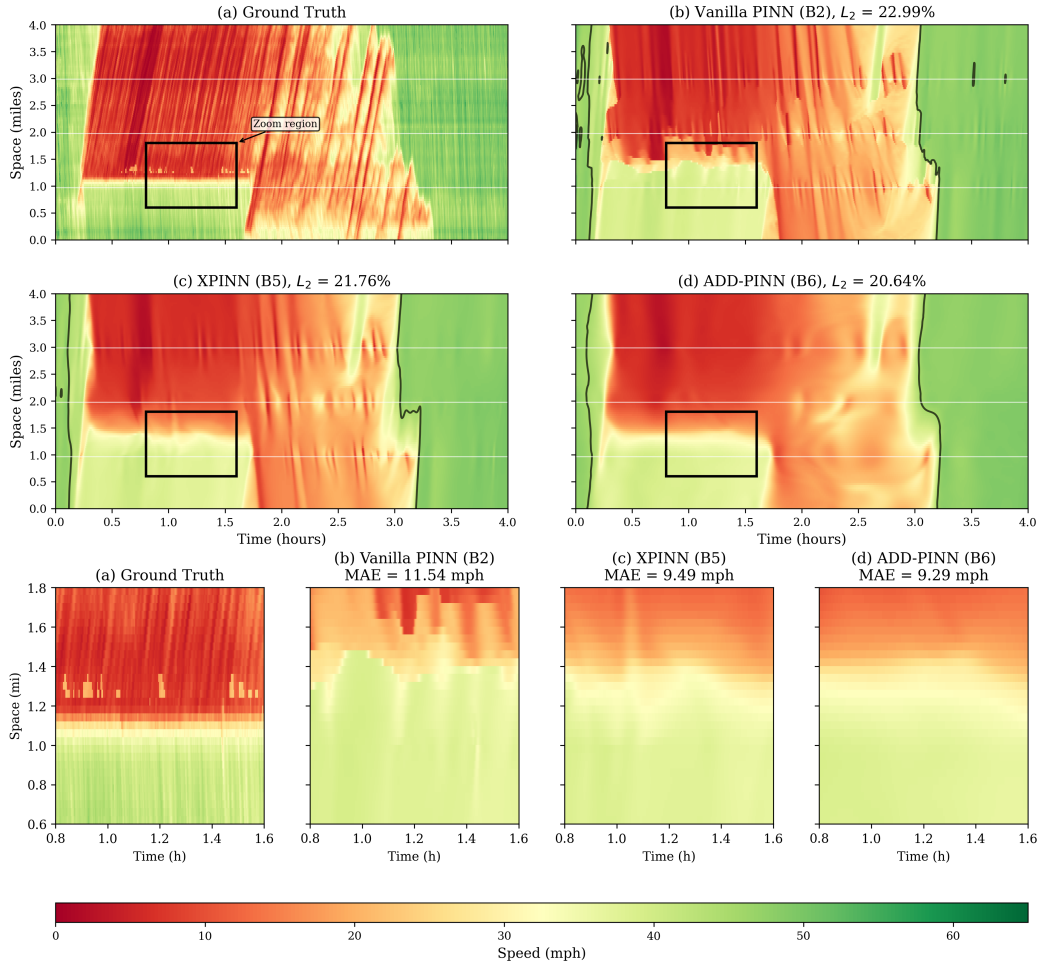


Figure 3: Representative speed field reconstruction for 20221121 with 3 sensors. Panel (a) shows the ground truth. Panels (b), (c), and (d) show Vanilla PINN (B2), XPINN (B5), and ADD-PINN (B6), respectively. The black box marks the zoom region spanning 0.8 to 1.6 h and 0.6 to 1.8 mi, which contains the congestion core. The 45 mph contour is overlaid on panels (b) to (d). All neural estimators recover the large-scale structure of the speed field, but the continuous function approximation smooths the sharpest gradients relative to the ground truth. In the zoom region, the mean absolute error is 11.54 mph for B2, 9.49 mph for B5, and 9.29 mph for B6, indicating that ADD-PINN has the lowest zoom-region error among the compared neural estimators.

Figure 3 presents a representative sparse case from 20221121 with 3 sensors. The visual differences in the full-speed fields are subtle because all three PINN-based models recover the dominant corridor-scale pattern. The main distinction appears within the boxed congestion core, where ADD-PINN preserves the extent of the low-speed region more faithfully than Vanilla PINN and slightly more faithfully than XPINN. The error maps in Figure 4 provide a more spatially resolved comparison.

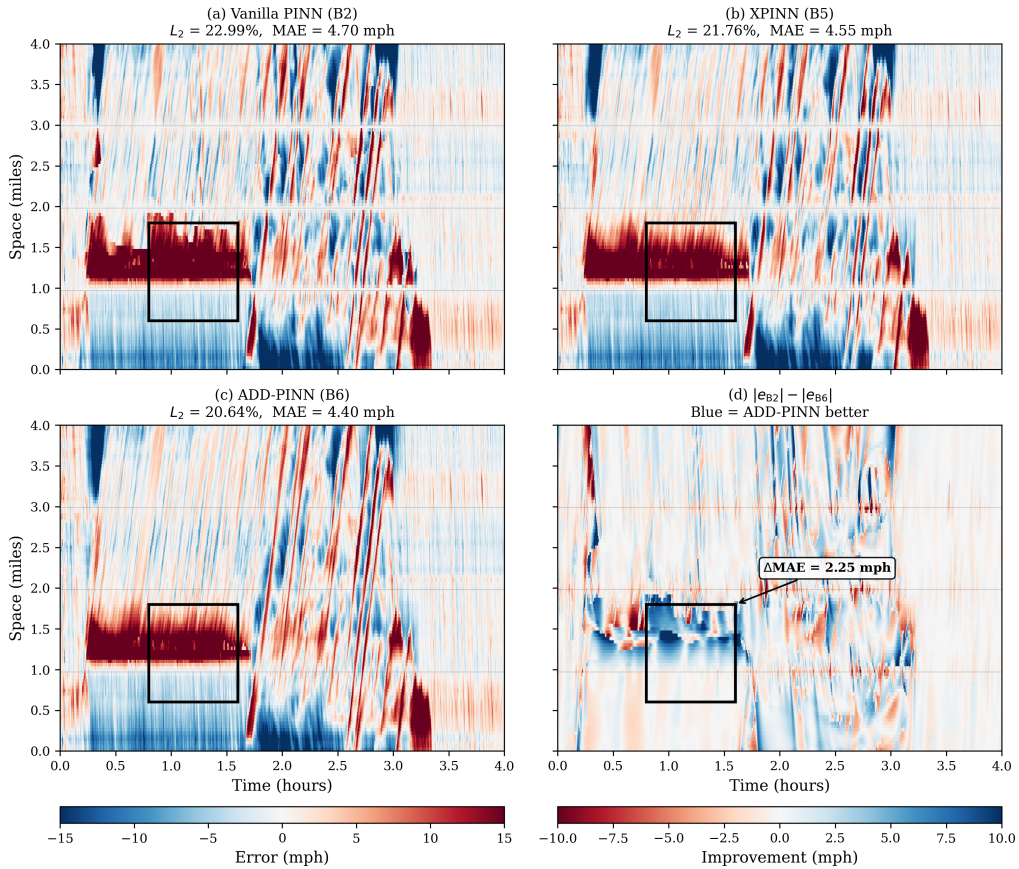


Figure 4: Pointwise error maps for the representative case in Figure 3. Panels (a), (b), and (c) report the signed speed error for Vanilla PINN (B2), XPINN (B5), and ADD-PINN (B6), respectively. Panel (d) shows the improvement map $|e_{B2}| - |e_{B6}|$, where blue indicates that ADD-PINN yields lower absolute error than Vanilla PINN. The full field mean absolute error is 4.70 mph for B2, 4.55 mph for B5, and 4.40 mph for B6. In the zoom region, the mean absolute improvement of ADD-PINN over Vanilla PINN is 2.25 mph.

Figure 4 reveals where the improvement is realized. In the congested zone below 30 mph, which occupies 54.8% of the domain in this representative case, ADD-PINN reduces mean absolute error from 5.55 mph for Vanilla PINN to 4.98 mph, an improvement of 0.57 mph. In the transition zone between 30 and 55 mph, the methods are broadly comparable. Panel (d) indicates that the blue improvement regions are concentrated along the congestion boundary and within the congestion core, rather than being uniformly distributed across the domain. This localization is consistent with the intended role of residual-guided decomposition: additional model capacity is allocated where the LWR residual is concentrated and where a single global network is most likely to oversmooth the solution.

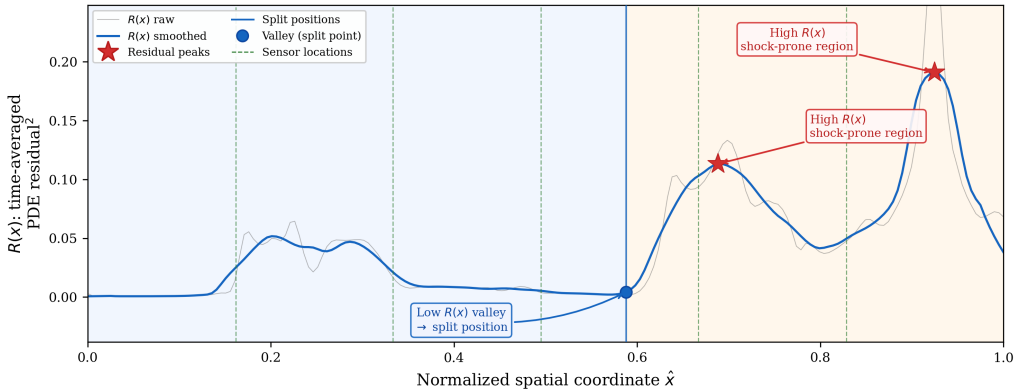


Figure 5: Spatial residual profile $R(x)$ for 20221121 with 5 sensors, computed from the coarse stage PINN before decomposition. Two dominant peaks appear near $x \approx 0.70$ and $x \approx 0.93$, identifying downstream shock-prone regions. The selected split at the low residual valley $x = 0.59$ separates the nearly smooth upstream free-flow region from the downstream transition region without cutting through the dominant residual peaks.

Figure 5 illustrates the residual-guided split mechanism. Upstream of the selected split, the residual remains close to zero, indicating that a single PINN is sufficient to represent the largely free-flow region. Downstream of the split, the residual rises sharply, indicating a shock-prone transition region that benefits from a dedicated child network. Choosing the boundary at the residual valley rather than at the residual peak prevents the artificial interface from bisecting the dominant transition itself and yields a more stable coupling between subdomains.

Taken together, Table 4 and Figures 3 to 5 indicate where the accuracy gains arise. The advantage of ADD-PINN is concentrated in the regime

where sparse fixed sensors leave large unobserved spatial gaps and the solution contains localized high-gradient transition regions. In this setting, residual-guided spatial decomposition provides a better inductive bias than both a single-domain PINN and the fixed space-time partition of XPINN. The smaller gains at $n_s = 7$ do not contradict this interpretation. Rather, they indicate that the marginal value of adaptive localization decreases as the reconstruction problem becomes more strongly data-constrained.

5.2. Decomposition Direction Ablation

We examine whether spatial-only decomposition is an effective default strategy for reconstructing fixed-sensor traffic in the settings studied. To test this question, we compare three variants within the same ADD-PINN framework: spatial-only, temporal-only, and space-time decomposition. The ablation uses two I-24 days (20221121 and 20221122), three sensor counts ($n_s \in \{3, 5, 7\}$), and 10 seeds per configuration, for a total of 120 runs.

For a representative case (20221121 with 5 sensors), spatial decomposition achieves the lowest relative L_2 error at 15.06%, temporal at 16.21%, and space-time at 15.25% (mean training time of 583 s, 329 s, and 931 s, respectively, averaged over 10 seeds). Temporal decomposition produces the highest error in five of six configurations. The exception is 20221122 with $n_s = 7$, where temporal decomposition is marginally better than spatial by 0.16 percentage points, a difference well within the seed-to-seed variability. Full results are reported in Appendix C.2.

Across all six configurations, spatial decomposition achieves the lowest error in five of six comparisons against temporal decomposition and in four of six against space-time decomposition, for a total of 9 of 12 pairwise comparisons. The three pairwise comparisons in which spatial decomposition does not rank first all involve the normal congestion day (20221122) at higher sensor counts ($n_s = 5$ and 7), where the differences among directions are below 0.2 percentage points. These comparisons suggest that the advantage of spatial decomposition is most pronounced under sparse sensing with localized transition regions, consistent with the data coverage asymmetry argument. Full results for all six configurations are reported in Appendix C.2.

Space-time decomposition achieves nearly identical mean accuracy to spatial (17.07% versus 17.02%, a difference of 0.05 percentage points) but requires 2.1 times the training time on average (998 s versus 474 s), because it creates four subdomains instead of two. The residual structure explains

why. The temporal residual profile $R(t)$ remains nearly flat across all ablation configurations, indicating little localization value in the time direction. By contrast, the spatial profile $R(x)$ exhibits pronounced peaks at shock-prone regions, indicating that the residual is strongly concentrated in space. This empirical pattern is aligned with the three theoretical arguments in Section 3.8. First, shockwave geometry is spatially localized, so spatial splitting directly isolates the sharp transition. Second, fixed sensors provide dense temporal traces but sparse spatial coverage, so temporal decomposition does not improve observability where information is missing. Third, the measured residual concentration is substantially stronger in space than in time, indicating that the coarse model errors are concentrated primarily in space in these evaluated cases. Figure 5 provides a representative example of this concentration, where the upstream region is nearly residual-free, and the downstream region contains the dominant transition structure.

5.3. Sensor Sensitivity Analysis

Table 5 and Figure 6 summarize how performance changes with sensor density, averaged across all five I-24 days. ADD-PINN consistently improves on Vanilla PINN, with the largest gain at the sparsest setting, $n_s = 3$, where the mean reduction is 2.22 percentage points. The improvement remains substantial for $n_s = 4$ and $n_s = 5$, then decreases to 1.04 percentage points at $n_s = 6$ and 0.63 percentage points at $n_s = 7$.

Table 5: Mean relative L_2 error (%) as a function of sensor count, averaged across all five I-24 datasets. Δ denotes the improvement of B6 over B2 in percentage points.

n_s	B2 (PINN)	B5 (XPINN)	B6 (Ours)	Δ (B2→B6)
3	21.00	20.43	18.78	+2.22
4	18.54	17.92	16.87	+1.67
5	17.52	16.65	15.79	+1.73
6	16.41	15.57	15.37	+1.04
7	15.15	13.88	14.52	+0.63

These results are relevant for freeway monitoring in under-instrumented corridors. In such settings, the estimator must reconstruct long unobserved spatial intervals from a small number of fixed-sensor traces. The widening gap in Figure 6 indicates that ADD-PINN provides the largest improvement in this evaluated sparse-sensing regime. The crossing at $n_s = 7$ should be interpreted as a scope condition rather than a contradiction. Under denser

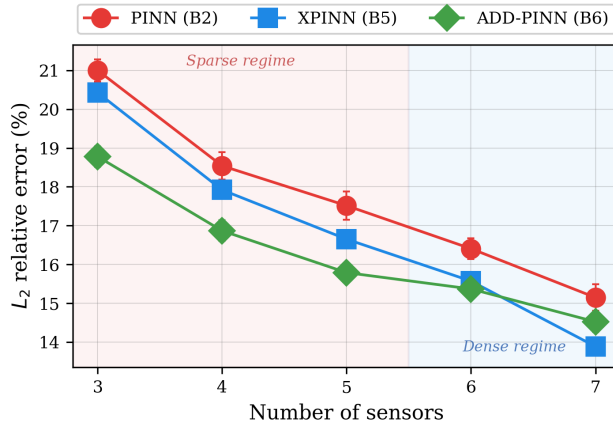


Figure 6: Mean relative L_2 error versus sensor count for Vanilla PINN (B2), XPINN (B5), and ADD-PINN (B6), averaged across the five I-24 days. Error bars indicate seed standard deviation.

virtual-sensor settings, the advantage of residual-guided spatial decomposition diminishes, and the fixed space-time partition of XPINN is no longer consistently disadvantaged.

5.4. Computational Efficiency

Table 6 compares mean accuracy and training time across all 25 I-24 configurations. ADD-PINN achieves the best average relative L_2 error at 16.26% while requiring 496 s of training time, compared with 1,189 s for XPINN. This 2.4 times speedup reflects both warm start and subdomain count: ADD-PINN uses one coarse stage and two warm-started child networks, whereas XPINN trains four subnetworks from scratch for the full budget. A complete separation of these effects remains a future component-ablation question.

Table 6: Mean accuracy and training time on I-24 MOTION, averaged across all 25 configurations (5 days \times 5 sensor counts) and 10 seeds (250 runs per method).

Method	L_2 (%)	Time (s)	Subdomains
B1 (NN)	34.71	39	1
B2 (PINN)	17.73	538	1
B3 (RAR)	16.90	115	1
B4 (Visc.)	16.81	249	1
B5 (XPINN)	16.87	1,189	4
B6 (Ours)	16.26	496	2

PINN+RAR (B3) is the fastest physics-informed baseline because, in addition to focusing training on high-residual regions through adaptive resampling, it processes a per-step collocation mini-batch rather than the full collocation pool. However, this speed comes at the expense of lower accuracy than ADD-PINN. For applications in which estimation quality is the primary concern, the overall accuracy-efficiency trade-off favors ADD-PINN. When runtime is severely constrained, and some loss of accuracy is acceptable, B3 remains a useful low-cost alternative.

5.5. Negative-Control Experiment on NGSIM

The NGSIM experiment, described in Section 4.1, serves as a negative-control case that delineates the operating regime of ADD-PINN. In contrast to the I-24 MOTION, the selected NGSIM interval contains diffuse congestion on a short corridor without a distinct localized transition boundary. In this experiment, the shock indicator did not trigger domain decomposition in any of the 50 NGSIM runs. The default ADD-PINN configuration, denoted B6*, retained the single-domain fallback. The result indicates that the adaptive mechanism withholds decomposition when the observed-data shock evidence does not support it.

Table 7: Results of negative-control experiment on NGSIM. B6* denotes the default shock-screened ADD-PINN, for which no decomposition was triggered in any run. B6† denotes a diagnostic decomposition-enabled variant. Values are the mean relative L_2 error (%) over 10 seeds.

n_s	B6* (Ours)	B5 (XPINN)	B6† (diagnostic)
3	18.75	19.14	19.67
4	16.76	16.86	17.29
5	15.35	15.51	16.26
6	13.15	13.21	14.62
7	12.25	12.45	13.94

Table 7 reports that B6* ranks first in all five sensor configurations, with an overall relative L_2 error of 15.25% and a mean training time of 123 s, compared with 668 s for XPINN. By contrast, B6† degrades to 16.36% and 273 s, ranking fifth overall. Full NGSIM results, including all baselines, are reported in Appendix C.3. The contrast between B6* and B6† supports the withholding role of the shock-screened fallback: when the selected NGSIM interval lacks a distinct localized transition boundary, the default mode retains

the single-domain estimator and outperforms the diagnostic decomposition-enabled variant. This experiment should be interpreted as a negative-control test of the fallback decision rather than as a full validation of the activation threshold on transition-rich I-24 cases. The diagnostic variant remains the most stable across seeds, with a standard deviation of 0.0209, indicating a stable but misaligned inductive bias rather than optimization instability. NGSIM therefore identifies a boundary of applicability and provides a negative-control test of the decomposition decision.

6. Discussion

The results support a narrower claim than *domain decomposition always helps PINNs*. For fixed-sensor freeway TSE under a first-order hyperbolic prior, decomposition is most beneficial when the observation geometry leaves long unobserved spatial intervals and the traffic field contains localized shock-prone transition regions. This interpretation is consistent with prior work on TSE observability, DD-PINN generalization, and PINN failure on transport-dominated PDEs (Seo et al., 2017; Hu et al., 2021; Huang and Agarwal, 2023; Karniadakis et al., 2021). The following subsections connect our empirical findings to the literature, clarify what is novel relative to XPINN and recent adaptive DD-PINNs, and state the main scope conditions of the present study.

6.1. Why Spatial Domain Decomposition Works for Fixed Sensor TSE

Three mechanisms help explain the findings of Section 5.2. First, spatial splitting reduces the local approximation burden created by spectral bias, gradient imbalance, and shock-prone LWR structure, consistent with PINN and conservation-law studies (Tancik et al., 2020; Wang et al., 2021; Krishnapriyan et al., 2021; Huang and Agarwal, 2023; Lei et al., 2025; Coutinho et al., 2023; De Ryck et al., 2024; Lorin and Novruzzi, 2024; Neelan et al., 2025; Wang et al., 2024; Wu et al., 2023). Second, fixed sensors provide dense temporal traces but sparse spatial coverage, so a spatial split targets the dominant observability gap (Seo et al., 2017; Wang and Papageorgiou, 2005; Wang et al., 2008; Zhao and Yu, 2024; Hu and Fan, 2024). Third, the coarse residual is more localized in space than in time; ADD-PINN uses this residual concentration diagnostically, not as an exact shock tracker, to allocate capacity where local refinement is most beneficial. This scope matches DD-PINN analyses showing that decomposition is effective when it simplifies

local functions sufficiently to outweigh interface costs and the reduced data per subdomain (Hu et al., 2021; Shukla et al., 2021; Moseley et al., 2023).

The I-24 and NGSIM results indicate that decomposition is useful when sparse sensing and localized transition structure coincide. The largest gains occur on the severe and incident I-24 days, whereas the NGSIM shock-screened mode retained the single-domain fallback in all 50 runs and ranked first across sensor configurations. When the diagnostic decomposition-enabled variant was used on NGSIM, the same architecture dropped to fifth overall. The split decision therefore carries regime information that has received limited attention in prior traffic DD-PINN studies (Huang and Agarwal, 2022; Shi et al., 2022, 2021; Lu et al., 2023).

XPINN is a useful DD baseline because it supports spatial, temporal, and space-time partitions within one unified framework (Jagtap and Karniadakis, 2020). The observed gains are consistent with a package-level design: residual-guided split placement, a minimal two-subdomain structure, parent-to-child warm start, and conservation-aware interface regularization. The contribution of ADD-PINN should therefore be interpreted as a traffic-specific decomposition workflow rather than as a claim that each component is new in isolation; component-level ablations remain a useful next step.

6.2. Traffic Engineering Implications

ADD-PINN is complementary to classical TSE methods. Extended Kalman filtering, adaptive smoothing, and variational or Hamilton-Jacobi methods remain better suited to online filtering, exact kinematic-wave interpretation, and uncertainty propagation (Wang and Papageorgiou, 2005; Wang et al., 2008; Treiber and Helbing, 2002; Daganzo, 2006; Canepa and Claudel, 2017), while ADD-PINN targets offline reconstruction from sparse fixed sensors with localized transition regions.

In the offline I-24 reconstruction setting, estimator design can shift the sensor-density/error trade-off. ADD-PINN with 4 sensors attains 16.87% relative L_2 error, lower than Vanilla PINN with 5 sensors at 17.52%, and ADD-PINN with 5 sensors attains 15.79%, lower than Vanilla PINN with 6 sensors at 16.41%. In these equally spaced virtual-sensor experiments, comparable errors are therefore reached with one fewer interior sensor in the examples above. This should not be interpreted as a direct recommendation for sensor deployment; rather, it suggests that model design can affect the cost-accuracy frontier in offline reconstruction.

Current training times are better suited to post hoc corridor reconstruction, incident forensics, daily monitoring, and archived reconstruction than to streaming estimation (Seo et al., 2017; Treiber and Helbing, 2002; Lu et al., 2023; Rempe et al., 2022). The NGSIM fallback behavior also suggests how the method can avoid unnecessary subdomain creation when evidence of localized transitions is weak.

6.3. Limitations and Future Work

The first limitation is model scope. We use LWR with a Greenshields closure and a fixed, pre-estimated v_f to isolate the adaptive decomposition in a simple setting where shock-related PINN failure is documented (Huang and Agarwal, 2023). This choice does not imply that the Greenshields closure or first-order deterministic physics is sufficient for all TSE tasks. Second-order, stochastic, heterogeneous, and jointly learned constitutive models may be more realistic for settings with lane-changing, ramps, or class-specific behavior and remain natural extensions beyond the present evaluation (Aw and Rascle, 2000; Aw et al., 2002; Zhang, 2002; Shi et al., 2022, 2021; Wong and Wong, 2002; Jabari and Liu, 2012, 2013; Yuan et al., 2021b; Wang et al., 2022).

A second limitation is numerical: the valley-based split rule is heuristic, and a low-residual valley may not provide the optimal interface placement when shocks move substantially over time. Because the interface formulation is a strong-form localization strategy rather than an exact shock tracker, future work should combine adaptive decomposition with weak-form or discontinuity-aware losses (De Ryck et al., 2024; Lorin and Novruzi, 2024; Neelan et al., 2025).

A complementary future direction is to formulate the LWR prior in the cumulative-count variable $N(x, t)$ rather than directly in (q, ρ) or speed. Newell’s cumulative-flow construction and Daganzo’s variational formulation show that kinematic-wave solutions can be represented through a continuous, piecewise differentiable cumulative-count function satisfying a Hamilton-Jacobi structure, so shocks appear as slope discontinuities rather than state-variable jumps (Newell, 1993a; Daganzo, 2005). Such a formulation may reduce the direct conflict between continuous neural approximators and discontinuous traffic states, but it would also change the observation model because fixed sensors provide point measurements of speed, flow, or occupancy rather than cumulative counts. Residual-guided split detection and parent-to-child warm start would remain conceptually complementary in that setting

because they operate on learned residual fields and network weights rather than on a specific choice of traffic state variable.

A third limitation is data scope and sensing mode. The formulation is lane-aggregated, single-corridor, and source-free, so ramp-influenced cells may not be fully represented by the LWR residual. The evidence should therefore be interpreted as same-corridor multi-day robustness, not cross-roadway generalization. The use of full-field normalization statistics and a pre-estimated v_f also fixes the present study as an offline reconstruction evaluation rather than an online deployment study. Broader validation is needed across corridors, incident types, ramps, junctions, and sensing mixes. Probe vehicles and other Lagrangian data are especially important because richer spatial coverage may alter observability and the preferred decomposition direction (Herrera and Bayen, 2010; Seo and Kusakabe, 2015; Canepa and Claudel, 2017; Rempe et al., 2022; Wang et al., 2022). Network-scale extensions require coordinated link partitions and ramp source terms (Usama et al., 2022; Lu et al., 2023).

A fourth limitation is benchmark scope. The baselines are neural estimators and DD-PINN variants rather than classical TSE filters, smoothing methods, or variational estimators. This design isolates the domain-decomposition contribution within the PINN family, but it does not establish superiority over established traffic-engineering estimators such as extended Kalman filtering, adaptive smoothing, or variational Hamilton-Jacobi reconstruction (Wang and Papageorgiou, 2005; Wang et al., 2008; Treiber and Helbing, 2002; Daganzo, 2006; Canepa and Claudel, 2017). Matched comparisons with these classical estimators are an essential complementary direction. The architecture, loss weights, shock threshold, and split-detection thresholds are also fixed protocol choices for fair relative comparison, not optimized deployment prescriptions. Sensitivity across corridors and sensing regimes remains for future work. Future work should also compare with operator-learning approaches and incorporate uncertainty quantification using Bayesian or uncertainty-aware PINN tools (Zhang et al., 2019; Yang et al., 2021).

7. Conclusion

This study proposed ADD-PINN, a two-stage residual-guided framework with shock-screened spatial decomposition for offline freeway reconstruction from sparse fixed sensors. The method first trains a coarse global PINN,

uses observed-data shock screening to retain a single-domain fallback when localized transition evidence is weak, uses the residual profile to place split boundaries when decomposition is enabled, initializes child networks from the parent solution, and applies conservation-aware coupling across fixed artificial interfaces.

The results support four main findings. First, ADD-PINN achieved the lowest relative L_2 error in 18 of 25 I-24 configurations and in 14 of 15 sparse-sensing cases. The NGSIM negative control exhibited complementary behavior: the shock indicator suppressed decomposition across all 50 runs, and the default single-domain fallback ranked first across all five sensor configurations. Second, spatial decomposition was the best-performing direction for fixed-sensor TSE in the studied regimes, attaining the lowest error in 9 of 12 pairwise direction comparisons; space-time decomposition matched spatial accuracy within 0.05 percentage points but required 2.1 times the training time. Third, ADD-PINN improved the accuracy-efficiency trade-off relative to XPINN, with a 2.4-times I-24 speed advantage and a 5.4-times NGSIM advantage when decomposition was withheld. Fourth, the evaluation covered five I-24 days, five sensor configurations, and ten seeds, yielding 1,500 I-24 runs across six methods.

Overall, ADD-PINN is most beneficial when sparse fixed sensing coincides with localized transition regions. The method should be interpreted as a PINN-family framework for offline freeway reconstruction rather than as a replacement for calibrated classical TSE estimators or as an online deployment method. Future work should extend ADD-PINN to richer traffic physics, network-scale corridors with ramps and junctions, online normalization and parameter estimation, matched comparisons with classical TSE estimators, uncertainty quantification, cumulative-count formulations, and weak-form treatments of shocks.

CRedit authorship contribution statement

Eunhan Ka: Conceptualization, Methodology, Software, Investigation, Writing – original draft, Visualization. **Ludovic Leclercq:** Investigation, Writing – review & editing. **Satish V. Ukkusuri:** Conceptualization, Methodology, Investigation, Resources, Writing – review & editing, Supervision.

Acknowledgments

This work is based upon the work supported by the National Center for Transportation Cybersecurity and Resiliency (TraCR) (U.S. Department of Transportation National University Transportation Center) headquartered at Clemson University, Clemson, South Carolina, USA. Any opinions, findings, conclusions, and recommendations expressed in this material are those of the author(s) and do not necessarily reflect the views of TraCR, and the U.S. Government assumes no liability for the contents or use thereof.

Declaration of competing interest

The authors declare that they have no known competing financial interests or personal relationships that could have appeared to influence the work reported in this paper.

Data availability

The full source code, processed datasets, and experimental configurations used in this study will be released at <https://github.com/eunhanka/add-pinn> upon acceptance. The I-24 MOTION trajectory data are available from Gloudemans et al. (2023). The NGSIM I-80 trajectory data are publicly available from the U.S. Department of Transportation Federal Highway Administration (USDOT, 2016); the processed NGSIM protocol follows prior traffic PINN studies (Huang and Agarwal, 2022).

Declaration of generative AI use

During the preparation of this work, the authors used ChatGPT (OpenAI) in order to assist with language refinement and LaTeX formatting. After using this tool, the authors reviewed and edited the content as needed and take full responsibility for the published article.

References

Aw, A., Klar, A., Rasle, M., Materne, T., 2002. Derivation of continuum traffic flow models from microscopic follow-the-leader models. *SIAM Journal on applied mathematics* 63, 259–278.

- Aw, A., Rascle, M., 2000. Resurrection of “second order” models of traffic flow. *SIAM journal on applied mathematics* 60, 916–938.
- Barreau, M., Aguiar, M., Liu, J., Johansson, K.H., 2021. Physics-informed learning for identification and state reconstruction of traffic density, in: 2021 60th IEEE Conference on Decision and Control (CDC), IEEE. pp. 2653–2658.
- Botvinick-Greenhouse, J., Ali, W.H., Benosman, M., Mowlavi, S., 2025. Ab-pinns: Adaptive-basis physics-informed neural networks for residual-driven domain decomposition. *arXiv preprint arXiv:2510.08924* .
- Canepa, E.S., Claudel, C.G., 2017. Networked traffic state estimation involving mixed fixed-mobile sensor data using hamilton-jacobi equations. *Transportation Research Part B: Methodological* 104, 686–709.
- Coutinho, E.J.R., Dall’Aqua, M., McClenny, L., Zhong, M., Braga-Neto, U., Gildin, E., 2023. Physics-informed neural networks with adaptive localized artificial viscosity. *Journal of Computational Physics* 489, 112265.
- Daganzo, C.F., 1994. The cell transmission model: A dynamic representation of highway traffic consistent with the hydrodynamic theory. *Transportation research part B: methodological* 28, 269–287.
- Daganzo, C.F., 2005. A variational formulation of kinematic waves: basic theory and complex boundary conditions. *Transportation Research Part B: Methodological* 39, 187–196. doi:10.1016/j.trb.2004.04.003.
- Daganzo, C.F., 2006. On the variational theory of traffic flow: well-posedness, duality and applications. *Networks and Heterogeneous Media* 1, 601–619. doi:10.3934/nhm.2006.1.601.
- De Ryck, T., Mishra, S., Molinaro, R., 2024. wpinns: Weak physics informed neural networks for approximating entropy solutions of hyperbolic conservation laws. *SIAM Journal on Numerical Analysis* 62, 811–841.
- Gludemans, D., Wang, Y., Ji, J., Zachar, G., Barbour, W., Hall, E., Cebelak, M., Smith, L., Work, D.B., 2023. I-24 motion: An instrument for freeway traffic science. *Transportation Research Part C: Emerging Technologies* 155, 104311.

- Greenshields, B.D., Bibbins, J.R., Channing, W., Miller, H.H., 1935. A study of traffic capacity, in: Highway research board proceedings, Washington, DC. pp. 448–477.
- Herrera, J.C., Bayen, A.M., 2010. Incorporation of lagrangian measurements in freeway traffic state estimation. *Transportation Research Part B: Methodological* 44, 460–481.
- Hu, X., Fan, Y., 2024. Sensor placement considering the observability of traffic dynamics: On the algebraic and graphical perspectives. *Transportation Research Part B: Methodological* 189, 103057.
- Hu, Z., Jagtap, A.D., Karniadakis, G.E., Kawaguchi, K., 2021. When do extended physics-informed neural networks (xpinns) improve generalization? arXiv preprint arXiv:2109.09444 .
- Hu, Z., Jagtap, A.D., Karniadakis, G.E., Kawaguchi, K., 2023. Augmented physics-informed neural networks (apinns): A gating network-based soft domain decomposition methodology. *Engineering Applications of Artificial Intelligence* 126, 107183.
- Huang, A.J., Agarwal, S., 2022. Physics-informed deep learning for traffic state estimation: illustrations with lwr and ctm models. *IEEE Open Journal of Intelligent Transportation Systems* 3, 503–518.
- Huang, A.J., Agarwal, S., 2023. On the limitations of physics-informed deep learning: Illustrations using first-order hyperbolic conservation law-based traffic flow models. *IEEE Open Journal of Intelligent Transportation Systems* 4, 279–293.
- Hugoniot, H., 1887. Mémoire sur la propagation du mouvement dans un fluide indéfini (premiere partie). *Journal de Mathématiques Pures et Appliquées* 3, 477–492.
- Jabari, S.E., Liu, H.X., 2012. A stochastic model of traffic flow: Theoretical foundations. *Transportation Research Part B: Methodological* 46, 156–174.
- Jabari, S.E., Liu, H.X., 2013. A stochastic model of traffic flow: Gaussian approximation and estimation. *Transportation Research Part B: Methodological* 47, 15–41.

- Jagtap, A.D., Karniadakis, G.E., 2020. Extended physics-informed neural networks (xpinns): A generalized space-time domain decomposition based deep learning framework for nonlinear partial differential equations. *Communications in Computational Physics* 28, 2002–2041.
- Jagtap, A.D., Kharazmi, E., Karniadakis, G.E., 2020. Conservative physics-informed neural networks on discrete domains for conservation laws: Applications to forward and inverse problems. *Computer Methods in Applied Mechanics and Engineering* 365, 113028.
- Ka, E., Xue, J., Leclercq, L., Ukkusuri, S.V., 2024. A physics-informed machine learning for generalized bathtub model in large-scale urban networks. *Transportation Research Part C: Emerging Technologies* 164, 104661.
- Karniadakis, G.E., Kevrekidis, I.G., Lu, L., Perdikaris, P., Wang, S., Yang, L., 2021. Physics-informed machine learning. *Nature Reviews Physics* 3, 422–440.
- Kingma, D.P., Ba, J., 2014. Adam: A method for stochastic optimization. *arXiv preprint arXiv:1412.6980* .
- Krishnapriyan, A., Gholami, A., Zhe, S., Kirby, R., Mahoney, M.W., 2021. Characterizing possible failure modes in physics-informed neural networks. *Advances in neural information processing systems* 34, 26548–26560.
- Lei, Y.Z., Gong, Y., Chen, D., Cheng, Y., Yang, X.T., 2025. Potential failures of physics-informed machine learning in traffic flow modeling: theoretical and experimental analysis. *arXiv preprint arXiv:2505.11491* .
- Lighthill, M.J., Whitham, G.B., 1955. On kinematic waves ii. a theory of traffic flow on long crowded roads. *Proceedings of the royal society of london. series a. mathematical and physical sciences* 229, 317–345.
- Lorin, E., Novruzi, A., 2024. Non-diffusive neural network method for hyperbolic conservation laws. *Journal of Computational Physics* 513, 113161.
- Lu, J., Li, C., Wu, X.B., Zhou, X.S., 2023. Physics-informed neural networks for integrated traffic state and queue profile estimation: A differentiable programming approach on layered computational graphs. *Transportation Research Part C: Emerging Technologies* 153, 104224.

- Lu, L., Meng, X., Mao, Z., Karniadakis, G.E., 2021. Deepxde: A deep learning library for solving differential equations. *SIAM Review* 63, 208–228.
- Luo, D., Jo, S.H., Kim, T., 2025. Progressive domain decomposition for efficient training of physics-informed neural network. *Mathematics* 13, 1515.
- Ma, X., Tao, Z., Wang, Y., Yu, H., Wang, Y., 2015. Long short-term memory neural network for traffic speed prediction using remote microwave sensor data. *Transportation Research Part C: Emerging Technologies* 54, 187–197.
- McClenney, L., Braga-Neto, U., 2023. Self-adaptive physics-informed neural networks using a soft attention mechanism. *Journal of Computational Physics* 474, 111722.
- Moseley, B., Markham, A., Nissen-Meyer, T., 2023. Finite basis physics-informed neural networks (fbpinns): a scalable domain decomposition approach for solving differential equations. *Advances in Computational Mathematics* 49, 62.
- Neelan, A.G., Bosco, F.S.D., Jarugumalli, N.S., Vedarethinam, S.B., 2025. Physics-informed neural networks: Bridging the divide between conservative and non-conservative equations. *arXiv preprint arXiv:2506.22413*.
- Newell, G.F., 1993a. A simplified theory of kinematic waves in highway traffic, part i: General theory. *Transportation Research Part B: Methodological* 27, 281–287. doi:10.1016/0191-2615(93)90038-C.
- Newell, G.F., 1993b. A simplified theory of kinematic waves in highway traffic, part ii: Queueing at freeway bottlenecks. *Transportation Research Part B: Methodological* 27, 289–303. doi:10.1016/0191-2615(93)90039-D.
- Peng, M., Tang, H., Kou, Y., 2025. Adversarial and self-adaptive domain decomposition physics-informed neural networks for high-order differential equations with discontinuities. *Engineering Applications of Artificial Intelligence* 145, 110156.

- Raissi, M., Perdikaris, P., Karniadakis, G.E., 2019. Physics-informed neural networks: A deep learning framework for solving forward and inverse problems involving nonlinear partial differential equations. *Journal of Computational physics* 378, 686–707.
- Rankine, W.J.M., 1870. Xv. on the thermodynamic theory of waves of finite longitudinal disturbance. *Philosophical Transactions of the Royal Society of London* , 277–288.
- Rempe, F., Franek, P., Bogenberger, K., 2022. On the estimation of traffic speeds with deep convolutional neural networks given probe data. *Transportation research part C: emerging technologies* 134, 103448.
- Richards, P.I., 1956. Shock waves on the highway. *Operations research* 4, 42–51.
- Seo, T., Bayen, A.M., Kusakabe, T., Asakura, Y., 2017. Traffic state estimation on highway: A comprehensive survey. *Annual reviews in control* 43, 128–151.
- Seo, T., Kusakabe, T., 2015. Probe vehicle-based traffic state estimation method with spacing information and conservation law. *Transportation Research Part C: Emerging Technologies* 59, 391–403.
- Shi, R., Mo, Z., Di, X., 2021. Physics-informed deep learning for traffic state estimation: A hybrid paradigm informed by second-order traffic models, in: *Proceedings of the AAAI Conference on Artificial Intelligence*, pp. 540–547.
- Shi, R., Mo, Z., Huang, K., Di, X., Du, Q., 2022. A physics-informed deep learning paradigm for traffic state and fundamental diagram estimation. *IEEE Transactions on Intelligent Transportation Systems* 23, 11688–11698. doi:10.1109/TITS.2021.3106259.
- Shukla, K., Jagtap, A.D., Karniadakis, G.E., 2021. Parallel physics-informed neural networks via domain decomposition. *Journal of Computational Physics* 447, 110683.
- Si, C., Yan, M., 2025. Initialization-enhanced physics-informed neural network with domain decomposition (idpinn). *Journal of Computational Physics* 530, 113914.

- Tancik, M., Srinivasan, P., Mildenhall, B., Fridovich-Keil, S., Raghavan, N., Singhal, U., Ramamoorthi, R., Barron, J., Ng, R., 2020. Fourier features let networks learn high frequency functions in low dimensional domains. *Advances in neural information processing systems* 33, 7537–7547.
- Treiber, M., Helbing, D., 2002. Reconstructing the spatio-temporal traffic dynamics from stationary detector data. *Cooperative Transportation Dynamics* 1, 3.1–3.24.
- Usama, M., Ma, R., Hart, J., Wojcik, M., 2022. Physics-informed neural networks (PINNs)-based traffic state estimation: An application to traffic network. *Algorithms* 15, 447.
- USDOT, 2016. Next generation simulation (ngsim) vehicle trajectories and supporting data. URL: <http://doi.org/10.21949/1504477>. [Dataset]. Provided by ITS DataHub through Data.transportation.gov. Accessed 2023-11-28.
- Wang, S., Sankaran, S., Perdikaris, P., 2024. Respecting causality for training physics-informed neural networks. *Computer Methods in Applied Mechanics and Engineering* 421, 116813.
- Wang, S., Teng, Y., Perdikaris, P., 2021. Understanding and mitigating gradient flow pathologies in physics-informed neural networks. *SIAM Journal on Scientific Computing* 43, A3055–A3081.
- Wang, Y., Papageorgiou, M., 2005. Real-time freeway traffic state estimation based on extended kalman filter: a general approach. *Transportation Research Part B: Methodological* 39, 141–167.
- Wang, Y., Papageorgiou, M., Messmer, A., 2008. Real-time freeway traffic state estimation based on extended kalman filter: Adaptive capabilities and real data testing. *Transportation Research Part A: Policy and Practice* 42, 1340–1358.
- Wang, Y., Zhao, M., Yu, X., Hu, Y., Zheng, P., Hua, W., Zhang, L., Hu, S., Guo, J., 2022. Real-time joint traffic state and model parameter estimation on freeways with fixed sensors and connected vehicles: State-of-the-art overview, methods, and case studies. *Transportation Research Part C: Emerging Technologies* 134, 103444.

- Wong, G., Wong, S., 2002. A multi-class traffic flow model—an extension of lwr model with heterogeneous drivers. *Transportation Research Part A: Policy and Practice* 36, 827–841.
- Wu, C., Zhu, M., Tan, Q., Kartha, Y., Lu, L., 2023. A comprehensive study of non-adaptive and residual-based adaptive sampling for physics-informed neural networks. *Computer Methods in Applied Mechanics and Engineering* 403, 115671.
- Wu, Y., Tan, H., Qin, L., Ran, B., Jiang, Z., 2018. A hybrid deep learning based traffic flow prediction method and its understanding. *Transportation Research Part C: Emerging Technologies* 90, 166–180.
- Yang, L., Meng, X., Karniadakis, G.E., 2021. B-pinns: Bayesian physics-informed neural networks for forward and inverse pde problems with noisy data. *Journal of Computational Physics* 425, 109913.
- Yuan, Y., Wang, Q., Yang, X.T., 2021a. Traffic flow modeling with gradual physics regularized learning. *IEEE Transactions on Intelligent Transportation Systems* 23, 14649–14660.
- Yuan, Y., Zhang, Z., Yang, X.T., Zhe, S., 2021b. Macroscopic traffic flow modeling with physics regularized gaussian process: A new insight into machine learning applications in transportation. *Transportation Research Part B: Methodological* 146, 88–110.
- Zhang, D., Lu, L., Guo, L., Karniadakis, G.E., 2019. Quantifying total uncertainty in physics-informed neural networks for solving forward and inverse stochastic problems. *Journal of Computational Physics* 397, 108850.
- Zhang, H.M., 2002. A non-equilibrium traffic model devoid of gas-like behavior. *Transportation Research Part B: Methodological* 36, 275–290.
- Zhang, J., Mao, S., Yang, L., Ma, W., Li, S., Gao, Z., 2024. Physics-informed deep learning for traffic state estimation based on the traffic flow model and computational graph method. *Information Fusion* 101, 101971. doi:10.1016/j.inffus.2023.101971.
- Zhao, C., Yu, H., 2024. Observer-informed deep learning for traffic state estimation with boundary sensing. *IEEE Transactions on Intelligent Transportation Systems* 25, 1602–1611. doi:10.1109/TITS.2023.3318299.

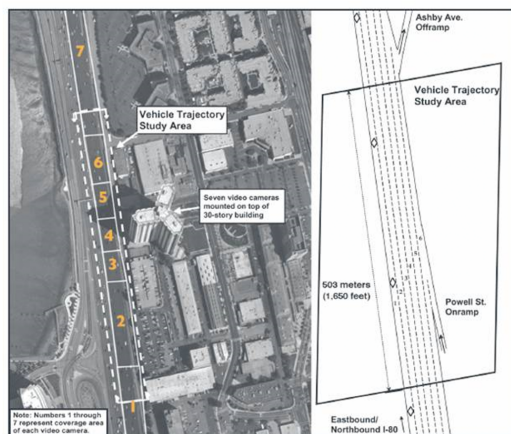
Appendix A. Notation Table

Table A.8: Notation used in the manuscript.

Symbol	Description	Symbol	Description
<i>Traffic flow variables and domain</i>			
$u(x, t)$	Speed field (mph)	Ω	Spatiotemporal domain
$\rho(x, t)$	Traffic density (vehicles/mile)	$\hat{x}, \hat{t}, \hat{u}$	Normalized coordinates and speed
$q(\rho)$	Flow as a function of density	x_{\min}, x_{\max}	Spatial domain bounds (feet)
v_f	Free-flow speed (mph)	T	Temporal domain extent (seconds)
ρ_{jam}	Jam density (vehicles/mile)	N	Number of spatial cells
u_{\max}	Maximum normalized speed (= 1)	n_s	Number of fixed sensors
<i>PDE, residual, and decomposition</i>			
$r(x, t)$	Normalized PDE residual	n	Number of subdomains
A, B, C	Nondimensionalization coefficients	θ	Network parameters
$R(x), R(t)$	Spatial / temporal residual profiles	\mathbf{W}	Fourier feature matrix
n_x, n_t	Residual evaluation grid dimensions	d_e	Fourier embedding dimension
K	Smoothing kernel size	σ	Fourier feature scale
<i>Loss functions and training</i>			
$\mathcal{L}_{\text{total}}$	Total training loss	$w_{\text{data}}, w_{\text{pde}}, w_{\text{int}}$	Fixed loss weights
$\mathcal{L}_{\text{data}}$	Data loss on sensor observations	w_j^{causal}	Causal weighting factor
\mathcal{L}_{pde}	PDE residual loss	ϵ	Causality parameter
\mathcal{L}_{int}	Interface coupling loss	E_{split}	Split epoch for decomposition
\mathcal{O}	Sensor observation set	E_{\max}	Maximum training epochs
N_{data}	Number of sensor observations	N_{pde}^s	Collocation points in subdomain s
<i>Interface quantities</i>			
s	Trainable shock speed	δ_{shock}	Shock detection threshold
\mathcal{L}_{RH}	Rankine-Hugoniot interface loss	$\lambda(\rho)$	Characteristic speed
$\mathcal{L}_{\text{entropy}}$	Entropy admissibility loss		

Appendix B. Supplementary Dataset Information

(a) NGSIM Data Site



(b) I-24 Motion Data Site

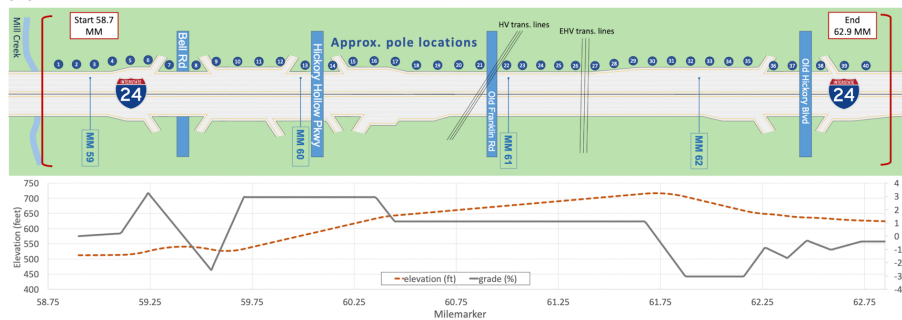


Figure B.7: Vehicle trajectory data collection sites used in this study. (a) NGSIM I-80 trajectory study area in Emeryville, California, covering a 1,600-ft freeway segment. (b) I-24 MOTION collection site along Interstate 24 near Nashville, Tennessee, covering the 4.2-mile corridor used in the primary experiments. (Sources: USDOT (2016) and Gloudemans et al. (2023)).

Appendix C. Supplementary Results

Appendix C.1. Statistical robustness for I-24 pairwise comparisons

Table C.9: Pairwise statistical comparison between ADD-PINN (B6) and each baseline on the 25 I-24 configuration means. W/L denotes configurations won and lost by B6. Δ is the mean improvement in relative L_2 error (percentage points) with 95% confidence interval. p_t : paired t -test; p_W : Wilcoxon signed-rank test; p_{Holm} : Holm-Bonferroni adjusted; d : paired Cohen’s d .

Comparison	W/L	Δ [95% CI] (pp)	p_t	p_W	p_{Holm}	d
B6 vs B1 (NN)	25/0	+18.44 [16.55, 20.34]	<.0001	<.0001	<.0001	4.02
B6 vs B2 (PINN)	25/0	+1.49 [1.15, 1.83]	<.0001	<.0001	<.0001	1.80
B6 vs B3 (RAR)	19/6	+0.90 [0.52, 1.27]	<.0001	<.0001	<.0001	0.99
B6 vs B4 (Visc.)	19/6	+0.80 [0.44, 1.17]	<.0001	.0001	.0001	0.90
B6 vs B5 (XPINN)	18/7	+0.67 [0.29, 1.04]	.0006	.001	.0006	0.73

Appendix C.2. Full decomposition direction ablation results

Table C.10: Full decomposition direction ablation results on two I-24 MOTION datasets with three sensor configurations. Each entry is the mean relative L_2 error (%) and the training time (seconds), both averaged over 10 random seeds. The lowest L_2 error per row is shown in **bold**. Spatial decomposition produces two subdomains, temporal decomposition produces two subdomains, and space-time decomposition produces four subdomains.

Date	n_s	Spatial		Temporal		Space-time	
		L_2	Time	L_2	Time	L_2	Time
20221121	3	20.69	392	21.48	380	20.89	901
20221121	5	15.06	583	16.21	329	15.25	931
20221121	7	14.07	519	14.75	328	14.12	1174
20221122	3	19.70	438	21.66	330	19.81	907
20221122	5	17.17	426	17.65	331	17.09	1029
20221122	7	15.41	484	15.25	338	15.28	1043
Mean		17.02	474	17.83	339	17.07	998

Appendix C.3. Full NGSIM supplementary results

Table C.11: NGSIM I-80 results: mean relative L_2 error (%) over 10 seeds. B6*: default shock-screened ADD-PINN; B6[†]: diagnostic decomposition-enabled variant.

n_s	B1 NN	B2 PINN	B3 RAR	B4 Visc.	B5 XPINN	B6* Ours	B6 [†] diagnostic
3	36.55	19.89	19.18	19.70	19.14	18.75	19.67
4	31.91	17.56	16.95	17.58	16.86	16.76	17.29
5	29.73	16.45	15.89	16.14	15.51	15.35	16.26
6	27.38	14.24	13.33	13.95	13.21	13.15	14.62
7	24.61	13.26	12.34	12.87	12.45	12.25	13.94

Appendix D. ADD-PINN Training Procedure

The full training pseudocode for ADD-PINN is given in Algorithm 1.

Algorithm 1 ADD-PINN Two-Stage Training

Require: Sensor data \mathcal{O} ; domain Ω ; split epoch E_{split} ; max epochs E_{max}
Ensure: Trained subdomain networks $\{\text{NN}_s\}_{s=1}^n$ and shock speeds $\{s_k\}$

- 1: Initialize single network NN_1 on Ω ; sample N_{pde} collocation points via LHS
- 2: Set fixed weights $w_{\text{data}} = 0.85$, $w_{\text{pde}} = 0.05$, $w_{\text{int}} = 0.10$
- 3: **for** epoch = 1 to E_{split} **do**
- 4: Compute $\mathcal{L}_{\text{data}} + \mathcal{L}_{\text{pde}}$ (with causal weighting) over mini-batches; update θ via Adam (lr = 10^{-3})
- 5: **end for**
- 6: **Shock detection:** compute data-driven shock indicators from \mathcal{O}
- 7: **Residual analysis:** compute residual profile $R(x)$ (default; or $R(t)$ / both for ablation, Section 3.5)
- 8: **if** shock detected **then**
- 9: **Split detection:** find peaks and valleys in $R(x)$; determine split positions from residual valleys
- 10: **else if** decomposition-enabled mode is requested **then then**
- 11: **Decomposition-enabled split:** partition into 2 subdomains using the selected residual valley in $R(x)$
- 12: **else**
- 13: **Single-domain fallback:** skip decomposition; the single coarse network proceeds to Stage 2 unchanged
- 14: **end if**
- 15: **if** decomposition was performed **then**
- 16: **Child creation:** create child networks; copy parent weights
- 17: **Child initialization:** fine-tune each child to match parent output (200 epochs)
- 18: **Interface setup:** create interfaces with trainable shock speeds $s_k \leftarrow 0$
- 19: **end if**
- 20: Rebuild optimizer: Adam (lr = 10^{-4}), StepLR(step= 5000, $\gamma = 0.9$)
- 21: Re-initialize collocation points for new subdomain structure
- 22: **for** epoch = $E_{\text{split}} + 1$ to E_{max} **do**
- 23: **for** each subdomain Ω_s **do**
- 24: Compute $\mathcal{L}_{\text{data}}^s$, $\mathcal{L}_{\text{pde}}^s$ with causal weighting
- 25: **end for**
- 26: Compute \mathcal{L}_{int} at all interfaces (Section 3.6)
- 27: $\mathcal{L}_{\text{total}} = w_{\text{data}}\mathcal{L}_{\text{data}} + w_{\text{pde}}\mathcal{L}_{\text{pde}} + w_{\text{int}}\mathcal{L}_{\text{int}}$
- 28: Update θ , $\{s_k\}$; clip gradients (max norm = 5.0)
- 29: **if** epoch mod 2,500 = 0 **then**
- 30: **RAR:** sample 5,000 candidates per subdomain; add top 2,500 by $|r|$
- 31: **end if**
- 32: **end for**
